On exploring the Hubbard Model with Ancilla Spins using Dynamical Mean-Field Methods and the Numerical Renormalization Group

Navid Roshani

Bachlor thesis

Chair of Theoretical Solid State Physics
Faculty of Physics
Ludwig-Maximilians-Universität München

Supervisor:
Prof. Dr. Jan von Delft

München, 29.09.2020

Über die Untersuchung des Hubbard Models mit Ancilla Spins mit Hilfe von Dynamischen Molekularfeldmethoden und der numerischen Renormalisierungsruppe

Navid Roshani

Bachlorarbeit

Lehrstuhl für theoretische Festkörperphysik
Fakultät für Physik
Ludwig-Maximilians-Universität München

Betreuer:
Prof. Dr. Jan von Delft

München, den 29.09.2020

Contents

1. Introduction

One of the central findings of condensed matter physics is Landau's Fermi liquid theory. The theory formulates how an interacting fermionic system can be described as a non-interacting system with renormalized parameters [21]. A fundamental result of this theory is Luttinger's theorem [6]. It states that the volume enclosed by a Fermi surface is directly proportional to the particle density.
Recently, Luttinger's theorem has becomes of great interest again. Studies of materials such as cuprate high T_c superconductors [10] and heavy fermion compounds [11] show that the theorem can be broken. They have in common that a transition between a conventional metal with large Fermi surface obeying Fermi Liquid theory to a metal with small Fermi surface which violates Luttinger's theorem can be observed. Hence, this so called pseudo-gap state has been of great significance in experimental as well as theoretical physics.
One new approach to this problem was given by Ya-Hui Zhang and Subir Sachdev. In their paper [1] they proposed a Hubbard model with two hidden ancilla qubit-spins per lattice site. Analyzing their Hamiltonian with a static mean-field approach they were able to reproduce the Fermi arcs found in ARPES experiments [12].
Still, the static mean field theory has its limits. Thats why this thesis will examine Zhang and Sachdevs Hamiltonian via the dynamical mean field theory (DMFT). Since its development [3] it has become one of the most successful theoretical tools to handle strongly correlated systems in a non-perturbative way. In the DMFT the complex quantum lattice is mapped self-consisted onto an effective impurity model, which is easier to solve. Moreover, it captures local quantum fluctuations, in contrast to the static case, which gives it its dynamical nature.
However, due to the local approach of the DMFT, it isn't possible to describe non-local correlations. As they are undoubtedly import for the analysis of correlated materials it is inevitable to expand the DMFT ideas to incorporate non-local effects. In this thesis, the dynamical cluster approximation (DCA) will be used to extend to DMFT [8]. By dividing up the Brillouin zone into smaller patches the DCA achieves to generate a k-dependence of the self-energy in contrast to the purely local one in the DMFT. This leads to a new self-consistency equation, which will take short-ranged correlations into account.
As both DMFT as well as DCA calculations need an impurity solver to perform their self-consistency procedure, the numerical renormalization group (NRG) will be used for this task. Since its invention by Ken Wilson [14], the NRG provides an iterative way to diagonalize effective impurity Hamiltonians. The resulting spectral function can be analyzed in

order to obtain information about the lattice.
All in all, this thesis will start with a brief summary of the DMFT in chapter 2. The main ideas will be taken and expanded in the DCA formalism in chapter 3. Afterwards in chapter 4, the NRG will be introduced as an impurity solver. Problems arising from combining both DMFT and NRG will be addressed in chapter 5. Then at last the Zhang-Sachdev Hamiltonian is introduced in chapter 6. Before going over to the results chapter 7 will deal with Luttinger's theorem. Presenting the results of the single site DMFT calculations the Hubbard model with no (chapter 8), one (chapter 9) and two (chapter 10) ancilla qubits per site will be considered in its respective chapters. The same approach will be used for the DCA calculations in chapter 11, 12 and 13. For all calculations the parameters will be varied in order to find possible phase transitions. Moreover, from chapter 10 onwards the theoretical filling after Luttinger's theorem will be calculated for the different results and compared to filling which was obtain from the numerical calculations. If a violation is found the Fermi surfaces will be reconstructed and a phase transition will be searched for. Chapter 14 will give a summary of the findings and an outlook for possible inquires into the model.

2. Dynamical Mean-Field Theory

The Dynamical Mean-Field Theory (DMFT) was first implemented in 1989 by D. Vollhart and W. Metzner during their work on the Hubbard model in infinite dimensions [3]. Later the basic DMFT framework was established by A. Georges and G. Kotliar in 1992 [4]. DMFT is an non-perturbative method to treat quantum lattice problems. Its dynamical nature is a result of freezing out the spatial fluctuations but still taking into account temporal quantum fluctuations. Reviews of the DMFT can be found in [5], [9] and [13]. For a better understanding of the basic ideas of the DMFT it is instructive to briefly take a look at classical mean-field theories.

2.1 Classical and Dynamical Mean field theory

An instructive example of the basic idea of the classical mean field theory can be found using the Ising model. It describes spins on a lattice experiencing nearest neighbour interactions and an external magnetic field. The Hamiltonian is defined in the following way:

$$H = -\frac{1}{2}\sum_{\langle i,j\rangle} J_{ij} S_i S_j - h\sum_i S_i \tag{2.1}$$

where $\sum_{\langle i,j\rangle}$ is the sum over all nearest neighbours with coupling constant J_{ij}. S_i is the Spin of the atom at site i. $\sum_i$ is a sum over all lattice sites while h is an external field. By implementing the classical mean field theory one tries to reduce the complex lattice model into a single site problem with effective parameters, that exhibit less degrees of freedom. In the case of the Ising model this can be achieved by the approximation $\Delta S_i \Delta S_j = 0$ and $\Delta S_i \equiv S_i - \langle S_i\rangle$:

$$\begin{aligned} H &= -\frac{1}{2}\sum_{\langle i,j\rangle} J_{ij}(\Delta S_i + \langle S_i\rangle)(\Delta S_j + \langle S_j\rangle) - h\sum_i S_i \\ &\approx -\frac{1}{2}\sum_{\langle i,j\rangle} J_{ij}(\langle S_i\rangle\langle S_j\rangle + \Delta S_i\langle S_j\rangle + \Delta S_j\langle S_i\rangle) - h\sum_i S_i = \\ &= -\frac{1}{2}\sum_{\langle i,j\rangle} J_{ij}(-\langle S_i\rangle\langle S_j\rangle + S_i\langle S_j\rangle + S_j\langle S_i\rangle) - h\sum_i S_i = \tilde{H} \end{aligned} \tag{2.2}$$

Additionally under the assumption of a translational invariant system $\langle S_i\rangle = \langle S_j\rangle \equiv \langle S\rangle$ and $J_{ij} = J$ the Hamiltonian simplifies to:

$$\begin{aligned}\tilde{H} &= -\frac{1}{2}\sum_{\langle i,j\rangle} J\left(-\langle S\rangle^2 + S_i\langle S\rangle + S_i\langle S\rangle\right) - h\sum_i S_i \\ &= \sum_i\left[-\sum_{nn}\frac{1}{2}J\left(-\langle S\rangle^2 + 2\cdot S_i\langle S\rangle\right) - hS_i\right] = \\ &= \sum_i\left[\sum_{nn}\left(\frac{1}{2}J\langle S\rangle^2 - JS_i\langle S\rangle\right) - hS_i\right] = \\ &= \frac{1}{2}zNJ\langle S\rangle^2 - \left[zJ\langle S\rangle + h\right]\sum_i S_i = \\ &= E_0 - h_{\text{eff}}\sum_i S_i\end{aligned} \tag{2.3}$$

$E_0 = \frac{1}{2}zNJ\langle S\rangle^2$ is an energy offset, with N being he total number of sites and z the cooradiantion number, so is thus physically irrelevant. $h_{\text{eff}}\sum_i S_i$ is the Hamiltonian of N noninteracting spins in an external field $h_{\text{eff}} = zJ\langle S\rangle + h$. With this result one arrives at the well known mean-field equation for the magnetization at finite temperature T:

$$\langle S\rangle = \tanh(\beta h + \beta zJ\langle S\rangle) \tag{2.4}$$

with β being $\beta = \frac{1}{k_B T}$. This equation has the form of a self consistency equation for the magnetization $\langle S\rangle$.
For an infinite coordination number z the approximation of neglecting correlated spin fluctuations becomes exact. However, to get meaningful results where physical quantities like the magnetization remain finite, the coupling J has to be rescaled:

$$J = \frac{J'}{z},\ J' = const. \tag{2.5}$$

Many of the basic ideas of the classical mean field theory can be adapted for the DMFT. In this case a complex quantum lattice model is mapped onto a quantum impurity model, which as to fulfill, similarly to the classical case, a self consistently equation. The whole lattice dynamics is captured by the local single-particle retarded Green's function:

$$G_{\alpha\beta}(t) = -i\Theta(t)\langle[c_\alpha(t), c_\beta^\dagger]_+\rangle_T \tag{2.6}$$

with creation/annihilation operator $c_\alpha/c_\beta^\dagger$ for electrons with quantum labels α, β for e.g. spins or orbitals and thermal average in the grand canonical ensemble $\langle ...\rangle_T$. For further information on the notation I refer to appendix A. When calculating the Green's function one will encounter a term for the self-energy $\Sigma(\omega)$. The approximation for DMFT lies in freezing out spatial fluctuations by assuming a local self-energy:

$$\begin{aligned}\Sigma_{i,j}(\omega) &\xrightarrow{z\to\infty} \Sigma(\omega)\delta_{i,j} \\ \Sigma_k(\omega) &\xrightarrow{z\to\infty} \Sigma(\omega)\end{aligned} \tag{2.7}$$

Again, this approximation becomes exact for an infinite coordination number [3]. To get finite results, the hopping altitude needs to be rescaled. In the following sections the Hamiltonians and Green's functions for the lattice model and impurity will be presented in detail.

2.2 Lattice model Hamiltonian and Green's function

The quantum lattice model has in general the form of

$$H_{\text{latt}} = \sum_{i\sigma}(\varepsilon_{d,\sigma} - \mu)n_{i\sigma} + \sum_i H_i^{\text{int}} + \sum_{\langle i,j\rangle\sigma} t_{ij}c_{i\sigma}^\dagger c_{j\sigma} \tag{2.8}$$

with creation/annihilation operator $c_{i\sigma}/c_{i\sigma}^\dagger$ of an electron on site i with spin σ. Furthermore, $n_{i\sigma}$ is the number-operater $n_{i\sigma} = c_{i\sigma}^\dagger c_{i\sigma}$.
$\sum_{\langle i,j\rangle}$ is a sum over all nearest neighbours with hopping altitude t_{ij}. μ is the chemical potential and ε_d being the flavour dependent energy.
H_i^{int} is an arbitrary interaction acting on site i. This term will be specified in Chapter 6.
To calculate the Green's function it is helpful to Fourier transform the Hamiltonian into momentum space, as in there the non-interacting part of the Hamiltonian is diagonal:

$$H_{\text{latt,k}} = \underbrace{\sum_{k\in 1.BZ}(\varepsilon_k - \mu)c_k^\dagger c_k}_{H^0} + \sum_i H_i^{int} \tag{2.9}$$

where H^0 is the non-interacting part of the Hamiltonian and ε_k is the dispersion relation. First, the non-interacting Green's function $G^0_{\text{latt,k}}$ will be calculated with an equation of motion Ansatz:

$$\omega\ G^0_{\text{latt,k}}(\omega) = \langle[c_k, c_k^\dagger]_+\rangle_T + G^0_{[c_k,H^0]_-,c_k^\dagger} \tag{2.10}$$

After solving this equation for the non interacting Green's function $G^0_{\text{latt,k}}(\omega)$ and inserting into the Dyson equation

$$G_{\text{latt,k}}(\omega)^{-1} = G^0_{\text{latt,k}}(\omega)^{-1} - \Sigma_k(\omega) \tag{2.11}$$

one arrives at the fully interacting Green's function for the lattice model

$$G_{\text{latt,k}}(\omega) = \frac{1}{\omega - \varepsilon_k + \mu - \Sigma_k(\omega)} \tag{2.12}$$

with $\Sigma_k(\omega)$ being the self energy. A full derivation with all steps in between can be found in Appendix B.
Using the the main DMFT approximation, of assuming the self energy is purely local, we arrive at:

$$G_{\text{latt,k}}(\omega) = \frac{1}{\omega + \mu - \varepsilon_k - \Sigma(\omega)} \tag{2.13}$$

This result will be now Fourier transformed to end up with an expression for the local on site Green's function.

$$\begin{aligned} G_{\text{latt}}(\omega) &= \frac{1}{N} \sum_{k \in 1.BZ} e^{ik(R_i - R_i)} G_{\text{latt}}(\omega) \\ &= \frac{1}{N} \sum_{k \in 1.BZ} \frac{1}{\omega + \mu - \varepsilon_k - \Sigma(\omega)} \\ &= \int_{-\infty}^{\infty} d\varepsilon \frac{\rho_0(\varepsilon)}{\omega + \mu - \varepsilon_k - \Sigma(\omega)} \end{aligned} \tag{2.14}$$

Here N denotes the number of k-points in the 1. Brillouin zone and $\rho_0(\varepsilon)$ is the non-interacting density of states, which will be specified in Sec. 2.5.

2.3 Impurity model Hamiltonian and Green's function

The Hamiltonian of the quantum impurity model H_{im}, on which the lattice model is mapped on, as the general form of

$$H_{\text{im}} = H_{\text{imp}} + H_{\text{bath}} + H_{\text{hyb}} \ , \tag{2.15}$$

$$H_{\text{imp}} = \sum_{\sigma} (\varepsilon_d - \mu) d_\sigma^\dagger d_\sigma + H_{\text{int}} \ , \tag{2.16}$$

$$H_{\text{bath}} = \sum_{k\sigma} \varepsilon_k c_{k\sigma}^\dagger c_{k\sigma} \ , \tag{2.17}$$

$$H_{\text{hyb}} = \sum_{k\sigma} V_k (d_\sigma^\dagger c_{k\sigma} + h.c.) \ , \tag{2.18}$$

with H_{imp} being the impurity Hamiltonian, H_{bath} the bath Hamiltonian and H_{hyb} the hybridisation Hamiltonian.
H_{imp} (Eq.16) describes a single site impurity with the same local interaction H_{int} as the lattice model. $d_\sigma / d_\sigma^\dagger$ denote the annihilation/creation operators of an impurity electron with spin σ, ε_d is the local energy level of the impurity site and μ the chemical potential.
H_{bath} (Eq. 17) describes a non-interacting bath of electrons with dispersion relation ε_k and annihilation/creation operators $c_{k\sigma} / c_{k\sigma}^\dagger$ for bath electrons with momentum k.
H_{hyb} couples bath and impurity Hamiltonian with hybridization V_k, which characterizes the hopping amplitude of electrons hopping between impurity and bath.
To calculate the impurity Green's function one can use an equation of motion Ansatz, which yields:

$$G_{\text{im}}(\omega) = \frac{1}{\omega - \varepsilon_d + \mu - \Delta(\omega) - \Sigma_{\text{im}}(\omega)} \tag{2.19}$$

with $\Sigma_{\text{im}}(\omega)$ being the self-energy and $\Delta(\omega)$ being the hybridization function, that is defined as

$$\Delta(\omega) = \sum_k \frac{V_k^2}{\omega - \varepsilon_k} \tag{2.20}$$

with imaginary part

$$\Gamma(\omega) = -\text{Im}(\Delta(\omega)) = \pi \sum_k V_k^2 \, \delta(\omega - \varepsilon_k) \tag{2.21}$$

A full derivation can be found in Appendix C.

2.4 DMFT self-consistency procedure

To map the original quantum lattice onto the effective impurity model in a self consistent way, the requirements

$$G_{\text{latt}}(\omega) \stackrel{!}{=} G_{\text{im}}(\omega) \tag{2.22}$$

$$\Sigma_{\text{im}}(\omega) \stackrel{!}{=} \Sigma_{\text{latt}}(\omega) = \Sigma(\omega) \tag{2.23}$$

are set. Now a self-consistency equation can be formulated using (Eq. 2.19):

$$\begin{aligned} \Delta(\omega) &= \omega - \varepsilon_d + \mu - \Sigma_{\text{imp}} - G_{\text{im}}(\omega) \overset{\text{Eq. 2.22}}{\underset{\text{Eq. 2.23}}{=}} \\ &= \omega - \varepsilon_d + \mu - \Sigma(\omega) - G_{\text{latt}}(\omega) \end{aligned} \tag{2.24}$$

With the help of this equation an iterative process can be started wich lead to the self-consistent DMFT equation:

1. Calculate the on site lattice Green's function (Eq. 2.14)
2. Insert the solution of G_{latt} into (Eq. 2.24) to derive the hybridization function for the impurity model
3. Solve the impurity model, which results into a new local self-energy
4. Using the new local self-energy to continue with step 1

A few remarks regarding the iterative procedure. As the local self-energy $\Sigma(\omega)$ isn't defined at the start of the calculation, an arbitrary value is used like $\Sigma(\omega) = 0$. To solve the impurity model an impurity solver is needed. There are many different methods to do so, but in this thesis the Numerical Renormalization Group will be used. The whole iterative procedure will be continued until the value of the local self-energy doesn't change by a given precision ε, which is in this thesis $\varepsilon = 10^{-3}$

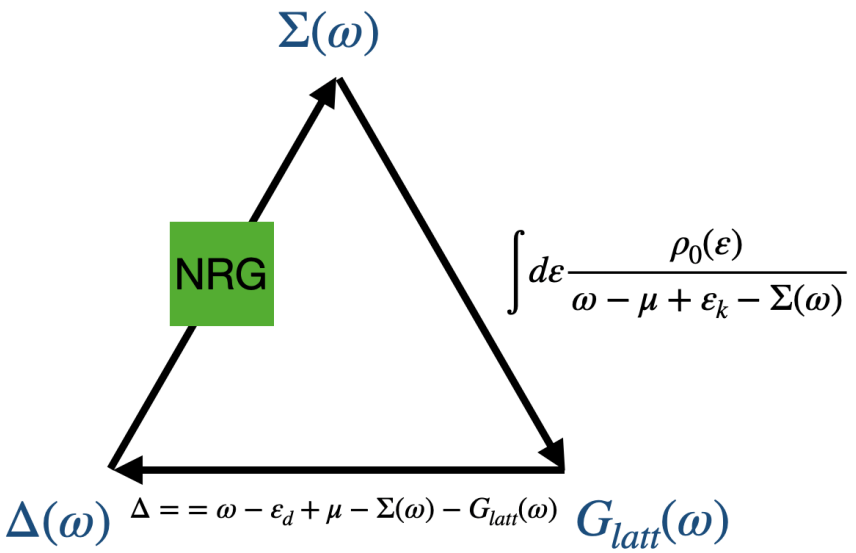

Figure 2.1: DMFT iterative self-consistency procedure. Starting with an arbitrary self-energy, the lattice Green's function is calculated. This expression will be inserted into the self-consistency equation yielding the hybridization $\Delta(\omega)$. Using the NRG as an impurity solver, the effective quantum impurity problem is solved, resulting in a new expression for the local self energy.

2.5 DMFT lattice model

As seen in section 2.2 the specific lattice geometry only enters via the non-interacting density of states (DOS) $\rho(\varepsilon)$ in (Eq. 2.14). In this thesis the Bethe lattice in the limit of infinite dimensions will be used for those equations. In z dimension the Bethe lattice is a graph where each site as z neighbours without containing any cycles. For the Bethe lattice in infinite dimensions, the DOS has a semi-elliptic form [13]:

$$\rho_0(\varepsilon) = \frac{2}{\pi D}\sqrt{1 - \left(\frac{\varepsilon}{D}\right)^2} \tag{2.25}$$

with D being the half the bandwidth and $\varepsilon \in [-D, D]$.
Therefore, if (Eq. 2.25) is inserted back in (Eq. 2.14) and the integral is being evaluated for the DOS, one will arrive at

$$G_{\text{latt}}(\omega) = \frac{2}{D^2}(\xi - \sqrt{\xi^2 - D^2}) \tag{2.26}$$

with $\xi = \omega - \Sigma(\omega) + \mu$. Rearranging the equation results in

$$\xi = \frac{D^2}{4} G_{\text{latt}}(\omega) + G^{-1}_{\text{latt}}(\omega) \tag{2.27}$$

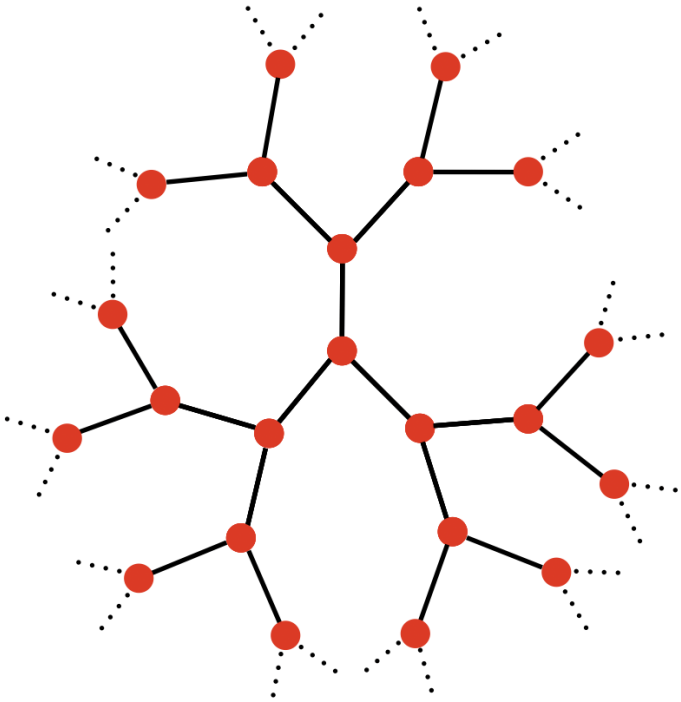

Figure 2.2: An example of a Bethe lattice with coordination number $z = 3$. Every node has exactly z neighbours, while the lattice doesn't contain any cycles

This equation can inserted back into the DMFT self-consitency equation (Eq. 2.24) in order to get an expression for $\Delta(\omega)$

$$\Delta(\omega) = \frac{D^2}{4} G_{\text{latt}}(\omega) - \varepsilon_d \tag{2.28}$$

Taking the imaginary part now, will result in an equation for Γ

$$\Gamma(\omega) = \pi \frac{D^2}{4} A_{ii}(\omega) \tag{2.29}$$

with $A_{ii}(\omega)$ being the local spectral function.

3. Dynamical cluster approximation

As the examination of short-range non-local correlations is of great interest the general DMFT ideas need to be expanded. In this thesis the dynamical cluster approximation (DCA) will be used to achieve the necessary corrections to the self-energy. This chapter will give an intuitive explanation for the origin of the DCA equations. For a mathematical derivation I refer to [8] and [9].

3.1 Derivation of self-consistency equation

In the DCA approach the Brillouin zone will be divided up into N_c equal sized patches. Each of those patches a have different self-energies, which is constant in its respective patch. Therefore, the new self-energies $\Sigma_{DCA}(\mathbf{k}, \omega)$ are $\vec{k}$-dependent.

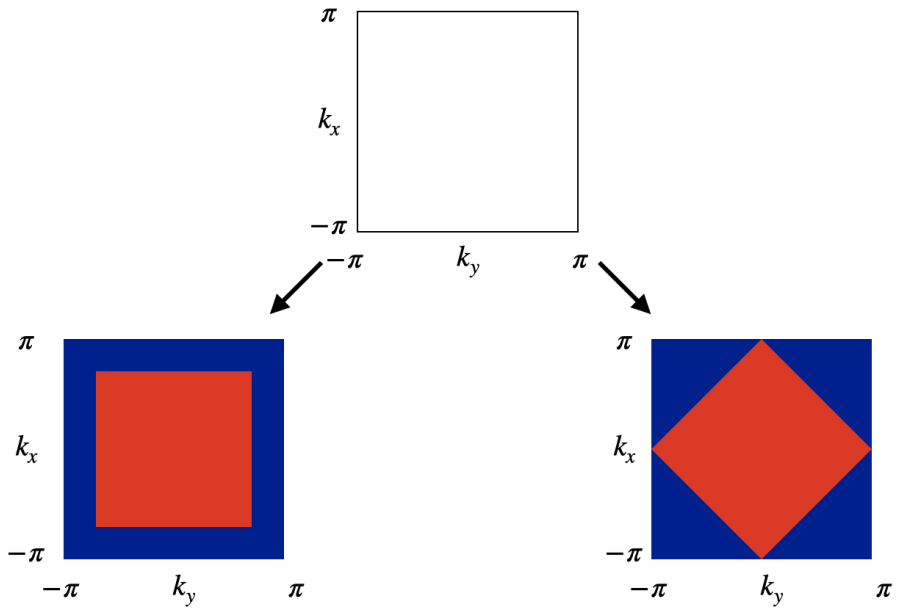

Figure 3.1: Two possible ways to divide up the Brillouin zone in $N_c = 2$ equal sized patches in the dynamical cluster approximation

Due to this new dependence, it isn't any more possible to assume the self-energy as purely local as it was done in the DMFT-approximation. In order to derive a self-consistency equation one has to calculate the average Green's function of the corresponding patch:

$$\bar{G}(\mathbf{K}_i, \omega) = \int_{P(\mathbf{K}_i)} \frac{d\mathbf{k}}{V_p} G(\mathbf{k}, \omega) \tag{3.1}$$

with $P(\mathbf{K}_i)$ denoting the patch represented by $\mathbf{K}_i$ and V_p being the volume of the patch. For $G(\mathbf{k}, \omega)$ the Dyson equation (Eq. 2.11) can now be inserted resulting in the self-consistency equation:

$$\bar{G}(\mathbf{K}_i, \omega) = \int_{P(\mathbf{K}_i)} \frac{d\mathbf{k}}{V_p} (G_0^{-1}(\mathbf{k}, \omega) - \Sigma_{DCA}(\mathbf{K_i}, \omega))^{-1} \tag{3.2}$$

For the DCA calculations in this thesis the Brillouin zone will be divided into $N_c = 2$ patches. The inner patch in the Brillouin will be called plus patch and the outer one minus patch.
For the choice of the interaction and single particle parameters I refer to [8]

3.2 Interpolation methods

As there is now one distinctive self-energy per patch, one has to find a way to combine both self-energies in order to calculate continous quantities for the full lattice. In this section two different interpolation methods will be presented as stated in [7].
The first method is the Σ-interpolation, where the self-energy is directly interpolated:

$$\Sigma_{\text{latt}}^{(\Sigma)}(\mathbf{k}, \omega) = \Sigma_+(\omega)\alpha_+(\mathbf{k}) + \Sigma_-(\omega)\alpha_-(\mathbf{k}) \tag{3.3}$$

with $\alpha_\pm = \frac{1}{2}\Big(1 \pm \frac{1}{2}[\cos(k_x) + \cos(k_y)]\Big)$ and $\Sigma_\pm$ being the self-energies of the plus and minus patch.
Another interpolation method is the M-interpolation, where first the cumulant $M \equiv (\omega + \mu - \Sigma)^{-1}$ is interpolated:

$$M_{\text{latt}}(\mathbf{k}, \omega) = \alpha_+(\mathbf{k}) \frac{1}{\omega + \mu - \Sigma_+(\omega)} + \alpha_-(\mathbf{k}) \frac{1}{\omega + \mu - \Sigma_-(\omega)} \tag{3.4}$$

with $\alpha_\pm$ being the above defined function. Now the self-energy can be derived from $M_{\text{latt}}(\mathbf{k}, \omega)$:

$$\Sigma_{\text{latt}}^{(M)}(\mathbf{k}, \omega) = \omega + \mu - M_{\text{latt}}(\mathbf{k}, \omega)^{-1} \tag{3.5}$$

3.3 DCA lattice model

For the DCA calculations a two dimensional square lattice will be used. The dispersion relation of such a lattice is defined as:

$$\varepsilon_k = -2t(\cos(k_x) + \cos(k_y)) - 4t' \cos(k_x)\cos(k_y) \tag{3.6}$$

with t being the nearest and t' being the next nearest neighbour hopping. For the patching of the Brillouin zone this thesis follows the scheme by [7]:

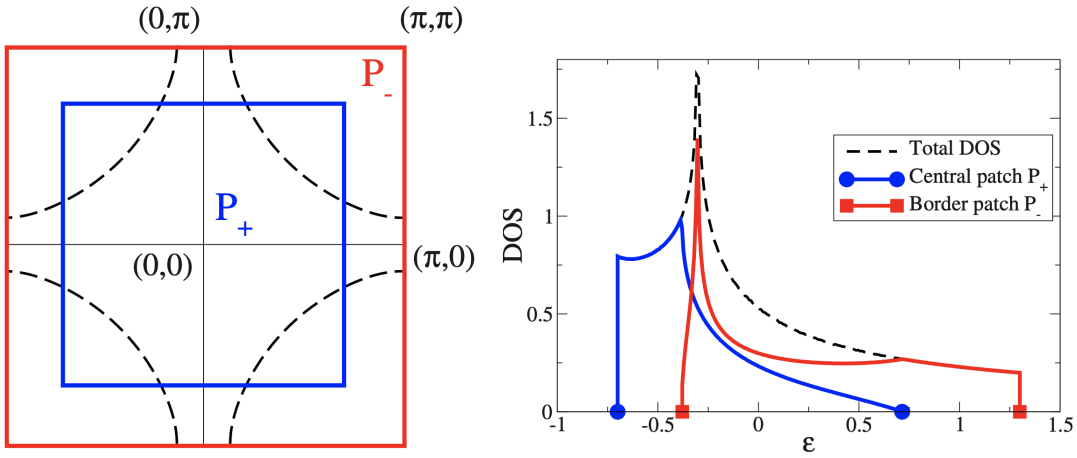

Figure 3.2: Left panel: Patching of the Brillouin zone into $N_c = 2$ patches. Th inner blue patch is called plus patch P_+, while the outer red one is the minus patch P_-. The dashed line denotes the Fermi surface at $U = 0$ with an electron doping at $\delta = 0.1$
Right panel: Density of states of the system. The red line corresponds to the DOS of the P_- and the blue line to the DOS of P_+. The dash line indicates the total DOS of a square lattice. Figures adapted from [7]

4. Numerical Renormalization Group

The Numerical Renormalization Group was developed by K.G. Wilson in the early 1970's [14] as non perturbative way to solve the Kondo model. Since then, it has developed into a reliable method to solve quantum impurity models in a non perturbative way. A detailed review of the NRG can be found in [15]

4.1 Summary of NRG process

Starting with a bath, with which the impurity interacts, a logarithmic discretization is applied. This leads to a set of states where low energy excitations are enhanced, which then can be mapped onto a semi-inifinte tight binding chain with exponentially decaying couplings called the Wilson chain. An iterative diagonalization is then used to solve the Wilson chain numerically. In the following sections this procedure will be presented in detail. For further insight I refer to [16],[13] and [18].

4.2 Hamiltonian

The impurity Hamiltonian has to general form of:

$$H = H_{\text{imp}} + \underbrace{\sum_{k\sigma} V_k (d_\sigma^\dagger c_{k\sigma} + h.c.)}_{H_{\text{hyb}}} + \underbrace{\sum_{k\sigma} \varepsilon_k c_{k\sigma}^\dagger c_{k\sigma}}_{H_{\text{bath}}} \tag{4.1}$$

with $c_{k\sigma}/c_{k\sigma}^\dagger$ being the annihilation/creation operators of a bath electron, while $d_\sigma/d_\sigma^\dagger$ are the annihilation/creation operators at the impurity. The coupling between bath and impurity systems are described by the hopping amplitudes V_k. As the conduction band has a finite band width of $[-D, D]$, ε_k is also confined in the same interval. Additionally, the chemical potential which is also defined in the interval $[-D, D]$ and will be set to $\mu = 0$. σ describes the spin index of the given bath/impurity electron.
For the NRG calculations the single impurity Anderson model (SIAM) can be used with Hamiltonian:

$$H_{\text{SIAM}} = H_{\text{imp}} + H_{\text{hyb}} + H_{\text{bath}} \tag{4.2}$$

$$H_{\text{imp}} = \sum_\sigma \varepsilon_d d_\sigma^\dagger d_\sigma + U d_\uparrow^\dagger d_\uparrow d_\downarrow^\dagger d_\downarrow \tag{4.3}$$

$$H_{\text{bath}} = \sum_{k\sigma} \varepsilon_k c^\dagger_{k\sigma} c_{k\sigma} \tag{4.4}$$

$$H_{\text{hyb}} = \sum_{k\sigma} V_k (d^\dagger_\sigma c_{k\sigma} + h.c.) \tag{4.5}$$

4.3 Logarithmic discretization

To discretize the conduction band a discretization parameter $\Lambda > 1$ will be introduced. With this parameter discretization points can be set in the conduction band at:

$$\epsilon_n^\pm = \pm\Lambda^{-n} D, n \in \mathbb{N} \tag{4.6}$$

These points partition the band into intervals

$$I_{\pm n} = \begin{cases} [-\epsilon_{|n|}, -\epsilon_{|n+1|}] & \text{for } -n \\ [\epsilon_{|n+1|}, \epsilon_{|n|}] & \text{for } +n \end{cases} \tag{4.7}$$

with decreasing width $l_n = \epsilon_n - \epsilon_{n+1} = D\Lambda^{-(n+1)}(\Lambda - 1)$ resulting in an enhanced resolution around the chemical potential. Each of this intervals $I_{\pm n}$ will be represented with an energy $\xi_{\pm n}$ that couples to the impurity with a strength of $\gamma_{\pm n}$.

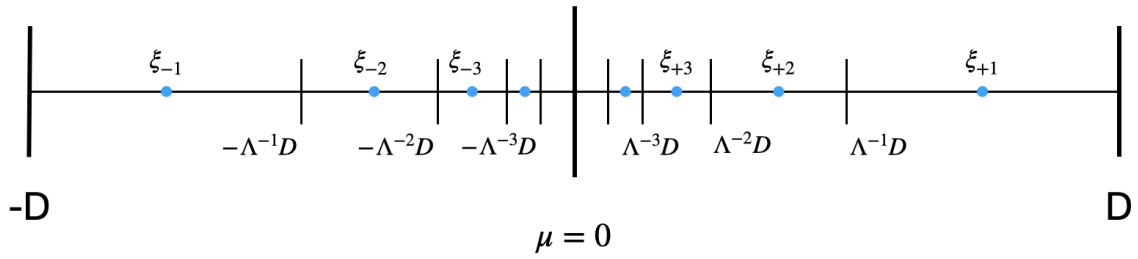

Figure 4.1: Logarithmic discretization of the conduction band of width $[-D, D]$. Here the discretization parameter is set to $\Lambda = 2$ which leads to intervals with energy $\xi_{\pm n}$.

Additionally, the discretization points can be shifted. To do so a shift parameter $z \in [0, 1)$ will introduced into (Eq. 3.6) resulting in:

$$\epsilon_n^\pm = \pm\Lambda^{-n-z} D \tag{4.8}$$

This so called z-shifting enhances the precision of the NRG results by averaging over the different shifts.

After the logarithmic discretization the Hamiltonian of the SIAM takes a new form:

$$\begin{aligned} H_{disc} &= H_{\text{imp}} + H'_{\text{bath}} + H'_{\text{hyb}} \\ H'_{\text{bath}} &= \sum_{n}^{\infty}\sum_{\sigma} \underbrace{\xi_{+n} c^{\dagger}_{+n\sigma} c_{+n\sigma}}_{\text{particle-like excitations}} + \underbrace{\xi_{-n} c^{\dagger}_{-n\sigma} c_{-n\sigma}}_{\text{hole-like excitations}} \\ H'_{\text{hyb}} &= \sum_{\sigma} (d^{\dagger}_{\sigma} (\sum_{\pm n} \gamma_{\pm n} a_{\pm n\sigma}) + (\sum_{\pm n} \gamma_{\pm n} a^{\dagger}_{\pm n\sigma}) d_{\sigma}) \end{aligned} \tag{4.9}$$

This form is also called star geometry due to the way the impurity couples to the different energy levels.

4.4 Mapping onto the Wilson chain

As the the bath and hybridization Hamiltonian (Eq.3.9) are quadratic they can be diagonalized exactly. First both terms will be written as a matrix:

$$H_{\text{star}} = H_{\text{hyb}} + H_{\text{bath}} = \begin{array}{c} \\ d^{\dagger} \\ a^{\dagger}_{+1} \\ \vdots \\ a^{\dagger}_{+\frac{N}{2}} \\ a^{\dagger}_{-1} \\ \vdots \\ a^{\dagger}_{-\frac{N}{2}} \end{array} \begin{array}{c} \begin{array}{ccccccc} d & a_{+1} & \cdots & a_{+\frac{N}{2}} & a_{-1} & \cdots & a_{-\frac{N}{2}} \end{array} \\ \begin{pmatrix} 0 & \gamma_{+1} & \cdots & \gamma_{+\frac{N}{2}} & \gamma_{-1} & \cdots & \gamma_{-\frac{N}{2}} \\ \gamma_{+1} & \xi_{+1} & & & & & \\ \vdots & & \ddots & & & & \\ \gamma_{+\frac{N}{2}} & & & \xi_{+\frac{N}{2}} & & & \\ \gamma_{-1} & & & & \xi_{-1} & & \\ \vdots & & & & & \ddots & \\ \gamma_{-\frac{N}{2}} & & & & & & \xi_{-\frac{N}{2}} \end{pmatrix} \end{array} \tag{4.10}$$

As this matrix is hermitian one can use Lanczos algorithm [17] to tridiagonalize it. Using this scheme the resulting matrix reads:

$$H_{\text{chain}} = \begin{array}{c} \\ d \\ f^{\dagger}_{0} \\ f^{\dagger}_{1} \\ f^{\dagger}_{2} \\ \vdots \\ f^{\dagger}_{N} \end{array} \begin{array}{c} \begin{array}{ccccccc} d & f_0 & f_1 & f_2 & \cdots & f_N \end{array} \\ \begin{pmatrix} \varepsilon_d & t_{\text{imp}} & & & & \\ t_{\text{imp}} & \varepsilon_0 & t_0 & & & \\ & t_0 & \varepsilon_1 & t_1 & & \\ & & t_1 & \varepsilon_2 & \ddots & \\ & & & \ddots & \ddots & \\ & & & & & \varepsilon_N \end{pmatrix} \end{array} = \tag{4.11}$$

$$\sum_{\sigma} t_{\text{imp}} (d_{\sigma} f^{\dagger}_{0\sigma} + h.c.) + \sum_{\sigma} \Big[\sum_{l=0}^{N-1} t_l (f^{\dagger}_{l\sigma} f_{(l+1)\sigma} + h.c.) + \sum_{l=0}^{N} \varepsilon_l f^{\dagger}_{l\sigma} f_{l\sigma} \Big]$$

If the impurity Hamiltonian is added to the chain Hamiltonian one arrives at the famous Wilson chain:

$$H_{\text{Wilson}} = H_{\text{imp}} + H_{\text{chain}} \tag{4.12}$$

In this semi-infinte tight-binding chain the first site represents the impurity which is coupled to the first bath site with strength t_{imp}. All following sites belong to the bath and couple to their nearest neighbours with hopping amplitude t_N. This hopping amplitude falls of exponentially for large n [13]:

$$t_N \overset{n\gg 1}{\rightarrow} \Lambda^{-\frac{N}{2}} \tag{4.13}$$

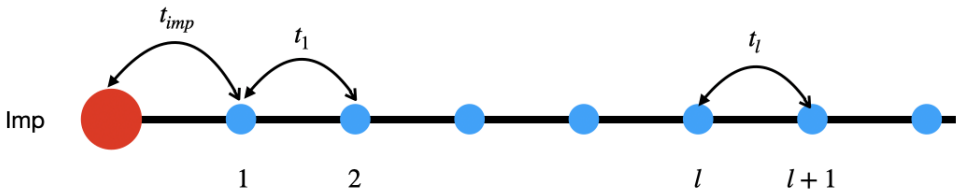

Figure 4.2: Graphical illustration of a Wilson chain. The impurity couples with the bath with strength t_{imp}. Each site after that belongs to the bath and has an exponentially decreasing coupling strength of t_N

4.5 Iterative Diagonalization

The Wilson chain has a reasonable form for an approximate diagonalization. To do so an iterative renomalization group (RG) procedure will be used which was invented by K.G. Wilson [14]. This procedure introduces a series of Hamiltonians $\hat{H}_N$ that approach H in the limit $N \rightarrow \infty$:

$$H = \lim_{N\rightarrow\infty} \Lambda^{-\frac{N}{2}} \hat{H}_N \tag{4.14}$$

with

$$\hat{H}_N = \Lambda^{\frac{N}{2}} \Big(H_{\text{imp}} + \sum_\sigma t_{\text{imp}} (d_\sigma f_{0\sigma}^\dagger + h.c.) + \sum_\sigma \Big[\sum_{l=0}^{N-1} t_l (f_{l\sigma}^\dagger f_{(l+1)\sigma} + h.c.) + \sum_{l=0}^{N} \varepsilon_l f_{l\sigma}^\dagger f_{l\sigma} \Big] \Big) \tag{4.15}$$

For simplicity reason the factor $\Lambda^{\frac{N}{2}}$ is applied to cancel the N-dependence of t_{N-1}. (Eq. 3.15) can now be used to formulate a recursion relation for $\hat{H}_{N+1}$:

$$\hat{H}_{N+1} = \sqrt{\Lambda} \hat{H}_N + \Lambda^{\frac{N}{2}} \sum_\sigma \Big[t_N (f_{N\sigma}^\dagger f_{(N+1)\sigma} + h.c.) + \varepsilon_{N+1} f_{N+1\sigma}^\dagger f_{N+1\sigma} \Big] \tag{4.16}$$

As the starting point of this recursive procedure the following equation

$$\hat{H}_0 = \Lambda^{\frac{1}{2}} \Big[H_{\text{imp}} + \sum_\sigma \Big(\varepsilon_0 f_{0\sigma}^\dagger f_{0\sigma} + t_{\text{imp}} (d_\sigma f_{0\sigma}^\dagger + h.c.) \Big) \Big] \tag{4.17}$$

will be used. With (Eq.3.16) and (Eq.3.17) it can be seen that they act as a renormalization group transformation R [19]:

$$\hat{H}_{N+1} = R(\hat{H}_N) \tag{4.18}$$

In general, to diagonalize the Wilson chain H_{Wilson}, $\hat{H}_0$ is diagonalized exactly and a set of eigenstates and eigenenergies are obtained. Then one continues with $\hat{H}_1$.
For a general RG step from $\hat{H}_N$ to $\hat{H}_{N+1}$, one will applies following scheme (Fig. 3.):

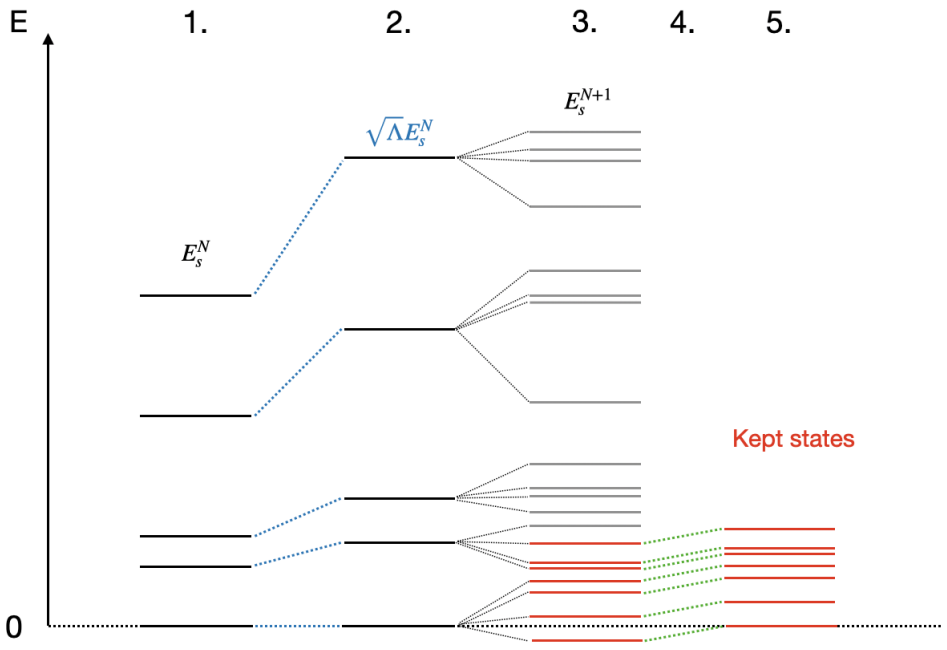

Figure 4.3: Iterative diagonalization procedure for $\hat{H}_N \to \hat{H}_{N+1}$: Starting with the eigenstates and eigenenergies of the previous iteration step (1.) one rescales them by a factor of $\sqrt{\Lambda}$ (2.). Then a new site is added which lifts the degeneracy of E_s^N through diagonalization of the new system (3.). The new eigenenergies E_s^{N+1} are then shifted so that the ground state has energy 0 (4.). In the last step (5.) the enlarged Hilbert space is truncated by discarding all states above a certain N_{keep}.

1. In the proceeding step $\hat{H}_N$ has been diagonalized. $|s\rangle_N$ are the eigenstates and E_s^N are the eigenenergies.

2. The eigenenergies are rescaled by a factor $\sqrt{\Lambda}$. This is done by the first term in (Eq.3.15).

3. Through the second and third term of (Eq.3.15) a new site of the Wilson chain is added. With this process the degeneracy of the eigenenergies are lifted. This result is diagonalized resulting in new eigenstates$|s\rangle_{N+1}$ and eigenenergies E_s^{N+1}.

4. For convenience the ground state energy is set to 0. This step is not mandatory.

5. As for each new site $|\sigma\rangle_{N+1}$ with dimension d added to the previous Hamiltonian $\hat{H}_N$ the dimension of the Hilbert space grows by a factor d. After a certain amount of iteration steps the whole procedure would become numerically infeasible as the dimension of the Hilbert space grows exponentially. Therefore a truncation scheme is applied where the eigenstates are kept to a specific number N_{keep}. This is possible as the high energy states have a small impact on the low-energy spectrum due to the weak perturbation compared to the energy of the high lying levels.

6. As a new $\hat{H}_{N+1}$ has been obtained, one goes back to step number 1.

This iterative process is continued until a specific energy resolution δE is reached.
As we truncate our Hilbert space for computational speed we are not able to construct a complete basis out of the pure result of the iterative diagonalization procedure. Remarkably, it is possible to construct such a complete basis from the discarded states. For a full review of this method I refer to [16] and [13].

5. Using NRG for the DMFT calculations

After we discussed the principles of the DMFT and NRG calculations, we will now try to combine both methods.

5.1 Calculation of the self-energy

As mentioned in section 2.4 the main use of the NRG is to calculate the self-energy the DMFT self-consistency procedure. one way to define the self-energy, which was also used in the derivations in Appendix C, is over the Dyson equation:

$$\Sigma(\omega) = G^0_{imp}(\omega)^{-1} - G_{imp}(\omega)^{-1} \tag{5.1}$$

Using this approach can lead to problems. While the non-interacting Green's function $G^0_{imp}(\omega) = \frac{1}{\omega - \varepsilon_d + \mu - \Delta(\omega)}$ can be calculated exactly, the interacting Green's function needs to be derived with the NRG. As we have a complete basis set we can calculate the spectral function via the Lehmann representation:

$$A_{B,C} = \sum_{n,m} \langle n| C |m\rangle \frac{e^{-\beta E_m}}{Z} \langle m| B |n\rangle \delta(\omega - (E_n - E_m)) \tag{5.2}$$

with Z being the norm of the density matrix $Z = \sum_m e^{-\beta E_m}$. As the spectral function is nothing else than the imaginary part of the Green's function $A_{A,B} = -\frac{1}{\pi}\mathrm{Im}(G_{A,B}(\omega))$ one can arrive at the real part by using the Kramers-Kronig relations. Adding both imaginary and real part together one arrives at $G_{\mathrm{imp}}(\omega)$. However, as this calculation of $G_{\mathrm{imp}}(\omega)$ displays numerical errors, taking the difference of an exact and an error-prone quantities can be detrimental to the accuracy of the result. This error can even increase over the course of the iterative procedure.
To circumvent this problem a different approach is used. The self energy can also be expressed as a ratio of two correlation functions [20]:

$$\Sigma(\omega) = \frac{F(\omega)}{G(\omega)} \tag{5.3}$$

with $G(\omega)$ being the on-site correlation function ($G_{imp}(\omega)$) and $F(\omega)$ being the two-particle retarded Green's function

$$F(\omega) = G_{[d,H_{int}]_-,d^\dagger} \tag{5.4}$$

In this case both quantities are calculated numerically, but as they are divided by each other only the relative remains which results into a numerically more stable procedure.

6. Zhang-Sachdev-Hamiltonian

In this thesis I will use the model which was introduced by Zhang and Sachdev. In their work [1] they used a standard Hubbard model with two extra ancilla qubits per square lattice site to describe the structure of the pseudogap metal state. These qubits are no physical degrees of freedom rather than theoretical tools which are used to reproduce the wished behaviour. The Hamiltonian goes as

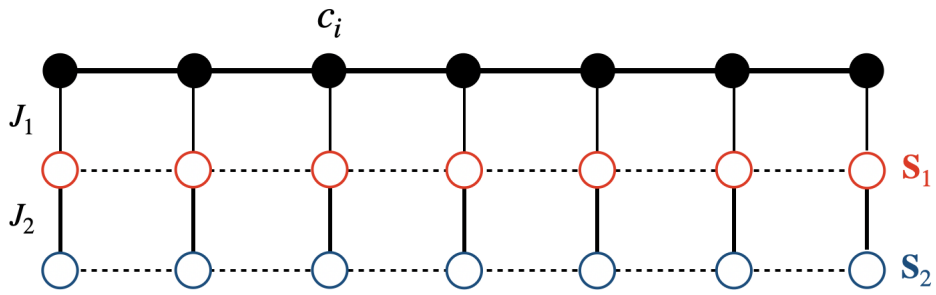

Figure 6.1: A Hubbard model of electrons $c_{i\sigma}$ coupled to two hidden square-lattice layers of ancilla qubits $\mathbf{S}_{i;1}$ and $\mathbf{S}_{i;2}$

$$H = H_U + H_a \tag{6.1}$$

with H_U being the Hubbard model of electrons $c_{i\sigma}$ on site i with spin σ

$$H_U = -\sum_{i,j} t_{i,j} c^\dagger_{i\sigma} c_{j\sigma} - \mu \sum_i c^\dagger_{i\sigma} c_{i\sigma} + U \sum_i n_{i\uparrow} n_{i\downarrow} \tag{6.2}$$

and H_a being the two hidden layers of ancilla spin $S = \frac{1}{2}$ qubits $\mathbf{S}_{i;1}$,$\mathbf{S}_{i;2}$

$$H_a = \frac{J_1}{2} \sum_i c^\dagger_{i\sigma} \sigma_{\sigma\sigma'} c_{i\sigma'} \cdot \mathbf{S}_{i;1} + J_2 \sum_i \mathbf{S}_{i;1} \cdot \mathbf{S}_{i;2} \tag{6.3}$$

with σ being the Pauli matrices.
This model will be treated using both the DMFT as well as the DCA. For the single-site DMFT calculations an adapted version of the single-impurity Anderson model, which was

introduced in section 4.2, will be used. In addition to the SIAM-Hamiltonian, terms will be added which represent the two ancilla spins:

$$H_{\text{im}}^{\text{DMFT}} = H_{\text{SIAM}} + \frac{J_1}{2} c_\sigma^\dagger \sigma_{\sigma\sigma'} c_{\sigma'} \cdot \mathbf{S}_1 + J_2 \mathbf{S}_1 \cdot \mathbf{S}_2 \tag{6.4}$$

with$c_\sigma / c_\sigma^\dagger$ being the annihilation/creation operators of the impurity.
For the DCA calculations on the other hand, a two-impurity Anderson model (2IAM) is needed due to the two different patches. Again, a term representing the ancilla spins will be added to the 2IAM:

$$\begin{aligned} H_{\text{im}}^{\text{DCA}} &= H_{\text{imp}} + H_{\text{hyb}} + H_{\text{bath}} + H_s \\ H_{\text{imp}} &= \sum_{l=1,2} (\varepsilon_d n_l + U n_{l\uparrow} n_{l\downarrow}) - t \sum_\sigma \left(d_{1\sigma}^\dagger d_{2\sigma} + h.c. \right) \\ H_{\text{hyb}} &= \sum_{lk\sigma} V_k \left[d_{lk\sigma}^\dagger c_{l\sigma} + h.c \right] \\ H_{\text{bath}} &= \sum_{lk\sigma} \varepsilon_k d_{lk\sigma}^\dagger d_{lk\sigma} \\ H_s &= \frac{J_1}{2} \sum_l c_{l\sigma}^\dagger \sigma_{\sigma\sigma'} c_{l\sigma'} \cdot \mathbf{S}_{l;1} + J_2 \sum_l \mathbf{S}_{l;1} \cdot \mathbf{S}_{l;2} \end{aligned} \tag{6.5}$$

7. Luttinger's theorem

A consequence of the findings of Fermi liquid is Luttinger's theorem, which was derived in 1960 by J. M. Luttinger [6]. The theorem states that the volume enclosed by a Fermi surface is directly probational to the particle density:

$$n_{\mathrm{LT}} = 2\frac{V_{\mathrm{FS}}}{(2\pi)^d} \tag{7.1}$$

with V_{FS} being the volume of a d-dimensional Fermi surface. The particle number n_{LT} only takes into account partially filled bands and is therefore defined in $n_{\mathrm{LT}} \in [0, 2]$. As shown in [2], it is necessary to incorporate spins into the Fermi surface to get an accurate result for the volume of the Fermi surface:

$$V_{\mathrm{FS}} = \frac{(2\pi)^d}{2}[\nu + 2N_S S] \tag{7.2}$$

with N_S being the number of spins S and ν being the total particle density.
As phases where Luttinger's theorem is violated are of great interest one must calculate the volume of the Fermi surface in order to compare with calculated fillings.

7.1 Calculating the volume of the Fermi surface

Starting with the interacting Green's function $G(k,\omega)^{-1} = \omega - \varepsilon_k + \mu - \Sigma(k,\omega)$ it is known [6] that

$$\begin{aligned} &G^{-1}(k,\omega=0) > 0, \text{occupied}, \\ &G^{-1}(k,\omega=0) < 0, \text{unoccupied} \end{aligned} \tag{7.3}$$

Therefore, the volume of the Fermi surface of a d-dimensional lattice can be defined as:

$$V_{\mathrm{FS}} = \int_{1.BZ} d^d k\ \Theta(G^{-1}(k,\omega=0)) = \int_{1.BZ} d^d k\ \Theta(-\varepsilon_k + \mu - \Sigma(k,0)) \tag{7.4}$$

This equation can be dividing through the volume of the first Brillouin zone $V_{1.\mathrm{BZ}}$ to result into the occupation predicted by Luttinger's theorem:

$$n_{\mathrm{LT}} = 2\frac{V_{\mathrm{FS}}}{V_{1.\mathrm{BZ}}} = \int_{1.\mathrm{BZ}} \frac{d^d k}{V_{1.\mathrm{BZ}}} \Theta(-\varepsilon_k + \mu - \Sigma(k,0)) \tag{7.5}$$

For the DCA calculations this is the final result. For the single-site DMFT calculations on the Bethe-lattice on the other hand Eq.(7.5) can be simplified due to the local nature of the self-energy:

$$\begin{aligned} n_{\mathrm{LT}} = 2\frac{V_{\mathrm{FS}}}{V_{1.\mathrm{BZ}}} = \int_{1.BZ} \frac{d^d k}{V_{1.\mathrm{BZ}}} \Theta(-\varepsilon_k + \mu - \Sigma(k,0)) = \\ \int_{-\infty}^{\infty} d\varepsilon \underbrace{\int_{1.BZ} \frac{d^d k}{V_{1.\mathrm{BZ}}} \delta(\varepsilon - \varepsilon_k)}_{\rho(\varepsilon)} \Theta(-\varepsilon + \mu - \Sigma(\omega = 0)) = \int_{-\infty}^{\mu - \Sigma(\omega=0)} d\varepsilon \ \rho(\varepsilon) \end{aligned} \tag{7.6}$$

8. Single site DMFT with $J_1 = 0$

Starting the study of the Zhang-Sachdev Hamiltonian at first the coupling of first ancilla qubit J_1 will be set to zero. This is done to find out how the physical behaviour of system changes when the ancilla qubits are bing added.
As J_1 describes the coupling between the lattice model and the qubits one can neglect the effects of the qubits on the lattice model when setting $J_1 = 0$. J_2 only influences the first ancilla qubit not the lattice model itself. Effectively, one works only with a Hubbard model in this calculations. As input parameters for the DMFT calculations the following values have been chosen:

N_{keep}	Λ	T	U	n	μ	t	n_z
2000	2	10^{-6}	[0,4]	1	$\frac{U}{2}$	0.5	2

Table 8.1: Values for single site DMFT calculations. N_{keep} describes the number of kept states before truncation, while Λ is the discretization parameter. T is the temperature and U is the strength of the Coulomb interaction. The filling per site is defined by n with corresponding chemical potential μ. t is the hopping amplitude and n_z describes the number of z-shifts.

The Hubbard model has at half-filling a so-called Mott-Hubbard metal-insulator transition (MIT). As in the Hubbard model

$$H = -\mu \sum_{i\sigma} n_{i\sigma} + \sum_{\langle ij \rangle \sigma} t c^{\dagger}_{i\sigma} c_{i\sigma} + U \sum_{i} n_{i\uparrow} n_{i\downarrow} \tag{8.1}$$

a competition between the kinetic and interaction part of the Hamiltonian arises this transition can be characterized as the ratio U/t of the Coulomb interaction strength and the hopping amplitude. If t is large compared to U the electrons can hopp freely between the different lattice sites, which corresponds to a metallic state of the system. For large U however, the electrons get localized due to the high energy cost of a doubly occupied state thus an insulator develops. This can be reproduced with the single site DMFT calculations:

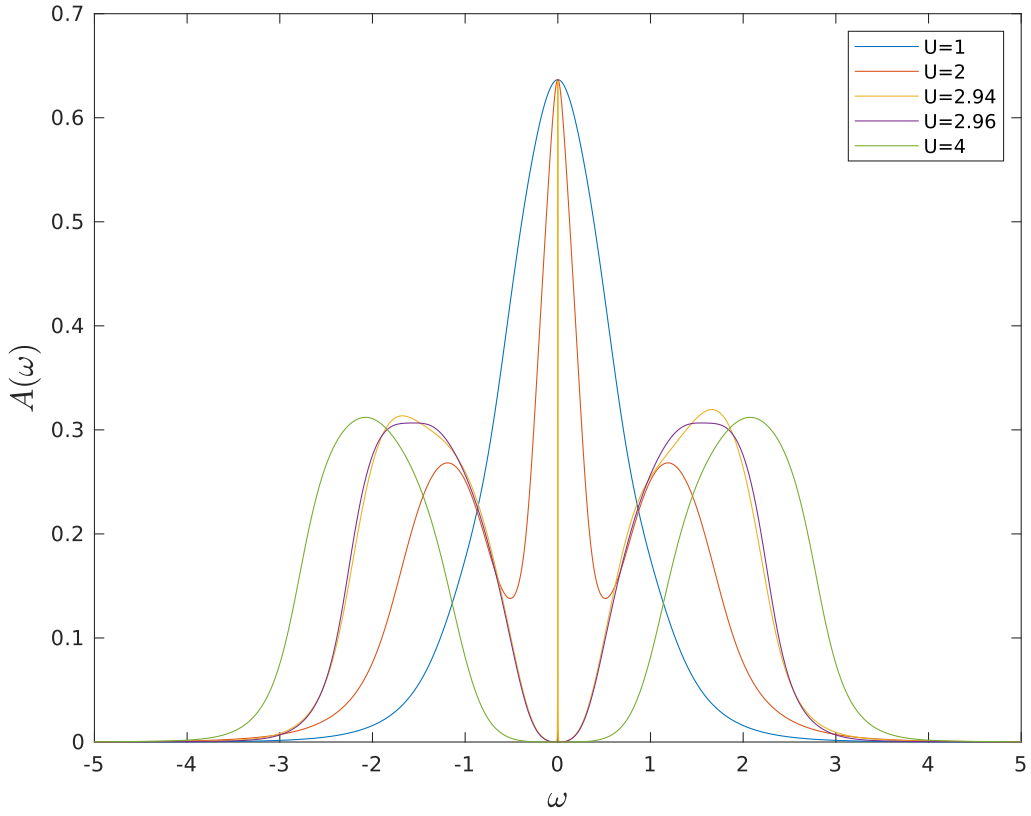

Figure 8.1: Spectral function of a Metal-insulator transition for the half-filled Hubbard-model for different values of U.

As it can be seen (Fig. 8.1) for small U the spectral function features a quasiparticle peak at $\omega = 0$, which is equivalent to the metallic phase. Dialing up the interaction results into a three peak structure with again a quasiparticle peak at $\omega = 0$ and two smaller peaks at $\pm U/2$. These peaks are describing atomic like excitations. A further increase of U leads to a reduction of the quasiparticle peak width, which ultimately vanishes above a certain U_c. For the performed calculations $U_c \approx 2.95$. The height of this peak is up to U_c a fixed value. After surpassing the critical $U_c < U$ only the two smaller peaks at $\pm U/2$ remain with a gap between them. The system is now in the insulating phase.

9. Single site DMFT with $J_2 = 0$

In this chapter the effect of one ancilla qubits per lattice site will be explored. To do so the coupling of the second qubit J_2 will be neglected. This corresponds to a Kondo lattice model. At first, the filling will be fixed at half-filling and, for different values of J_1, U will be varied in order to find a possible metal-insulator transition. Later, the filling will be changed while the interaction J_1 remains fixed.

9.1 J_1 and U variation at half-filling

For the result of the DMFT calculations following values will be chosen:

N_{keep}	Λ	T	U	J_1	J_2	n	μ	t	n_z
2000	2	1e-6	[1,10]	1	0	1	$\frac{U}{2}$	0,5	2

Table 9.1: Values for single site DMFT calculations of the lattice model at half-filling with a singled coupled ancilla qubit. J_1 is the coupling between the first ancilla qubit and the lattice electrons, while J_2 describes the coupling between the two ancilla qubits. The other parameters are defined as in Table 8.1.

As the lattice model will be set to half-filling, every site has on average one electron. The ancilla qubit which is now coupled to each site interacts with the electron through the coupling J_1. Together they form a singlet state. As all lattice electrons are bound, the lattice is in an insulating phase. Dialing up the Coulomb interaction U will only result into an increase of the charge gap (Fig. 9.1). Therefore, the lattice will always remain in an insulating phase for all values of U and J_1

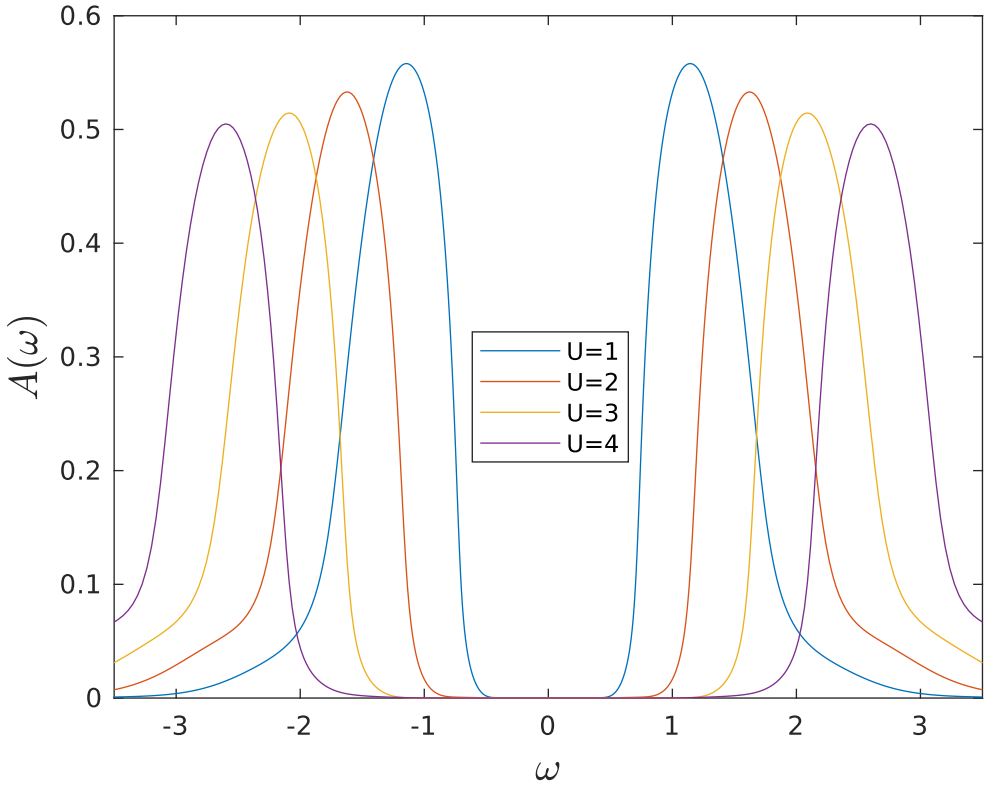

Figure 9.1: Variation of the Coulomb interaction U at $J_1 = 1$.

9.2 Variation of the filling

As there is no phase transition at half-filling as seen above, the filling of the lattice will be now varied while the coupling J_1 remaining fixed at $J_1 = 1$. The parameters are chosen as followed:

N_{keep}	Λ	T	U	J_1	J_2	μ	t	n_z
2000	2	1e-6	0	1	0	$[0, 10]$	0,5	2

Table 9.2: Values for single site DMFT calculations for the variation of the filling. The parameters are defined as in Table 8.1 and 9.1.

By changing the chemical potential we ensure the necessary shifts of the lattice filling. For small values of μ relative to J_1 the lattice is at half-filling and the lattice is in an insulating phase as in the previous section (Fig. 9.2 and 9.3). If now μ gets dialed up even further the spectral function develops a peak develops at $\omega = 0$ and the lattice becomes metallic. This is all due to the typical band structure of the Kondo lattice [21]. As there are two bands with a gap at $\mu = 0$ setting the chemical potential inside this gap will result

into the insulating state. For large enough μ one goes past this gap into the band so the lattice becomes metallic. For the parameters of this calculation (table 8.1) this happens at $\mu = 0.5$. .

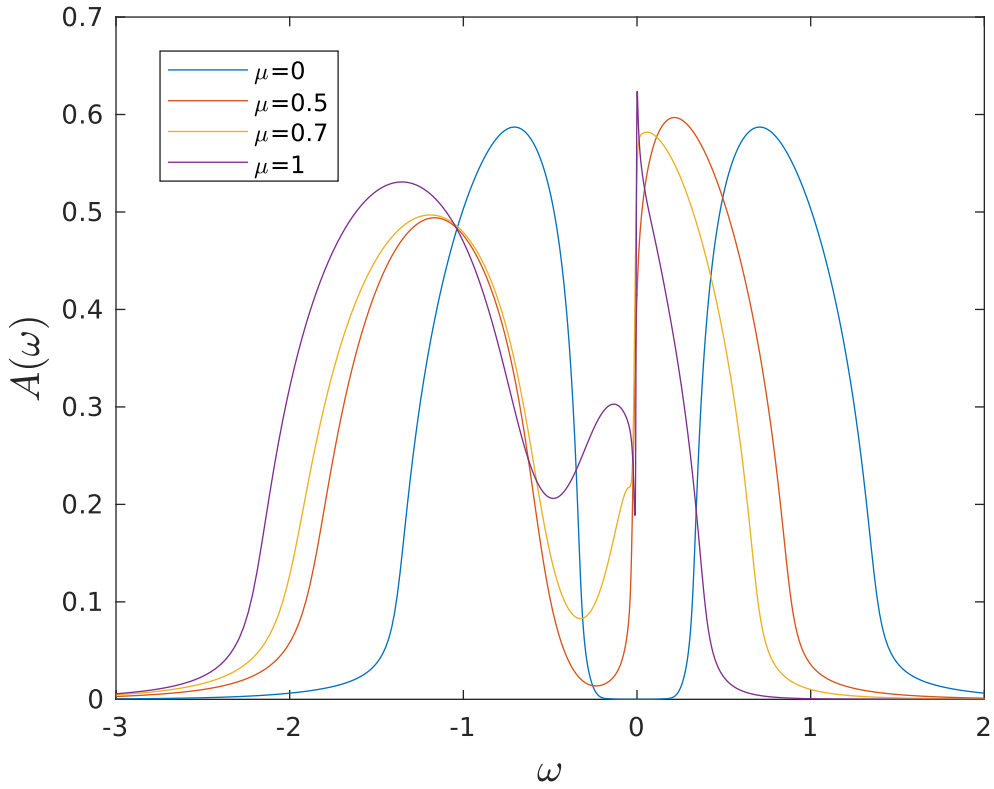

Figure 9.2: Variation of the filling with $J_1 = 1$ and $U = 0$. It can be seen that the lattice goes from an insulting to a metallic phase at $\mu = 0.5$.

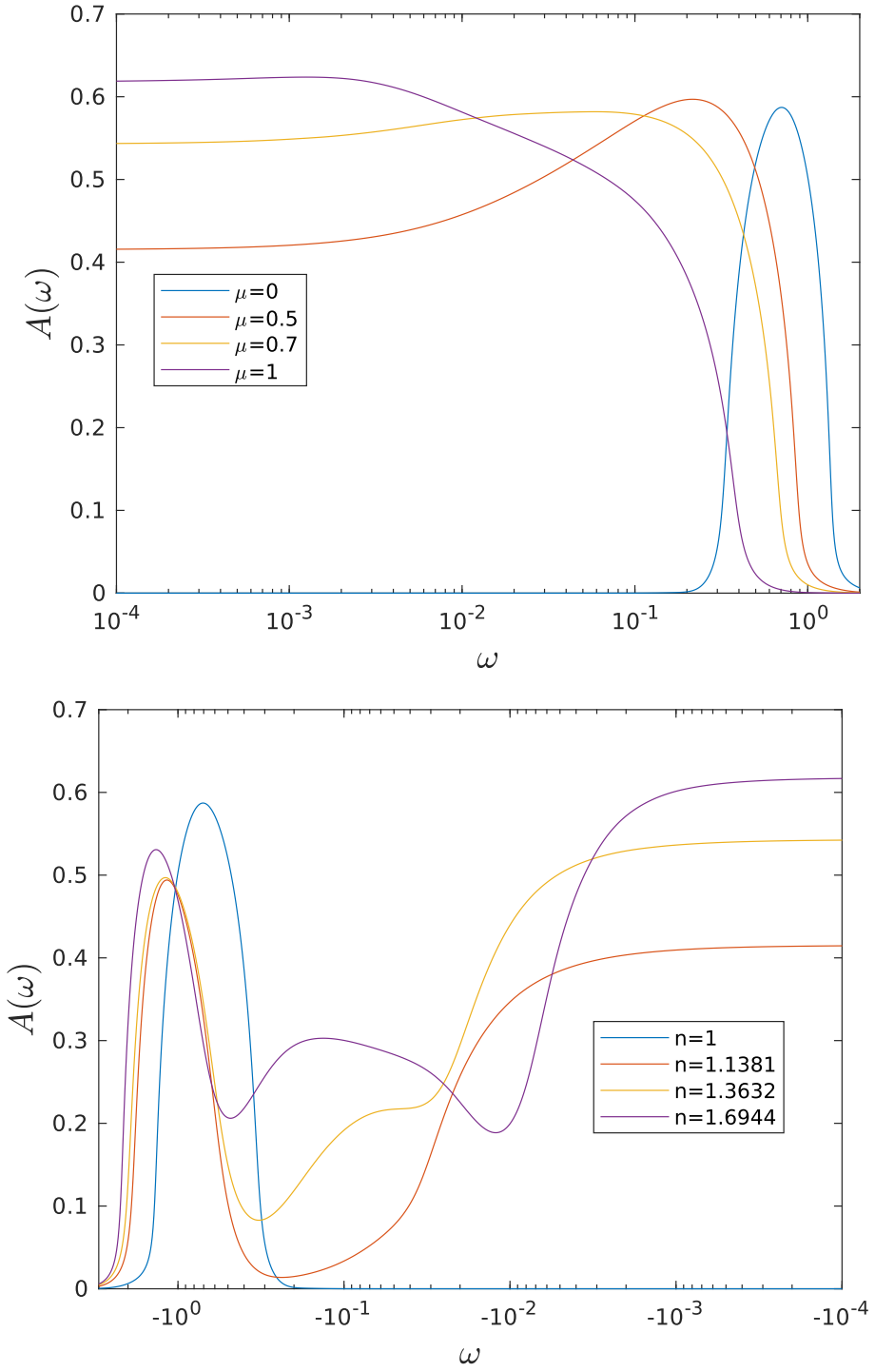

Figure 9.3: Variation of the filling with $J_1 = 1$ and $U = 0$. The upper panel shows the spectral function at different values of μ on a logarithmic ω axis in the interval $\omega \in [10^{-4}, 2]$. It can be seen that the lattice goes from an insulting to a metallic phase at $\mu = 0.5$. The lower panel shows the spectral function again on a logarithmic ω axis scale in the interval $\omega \in [-3, -10^{-4}]$. Here the legends show the filling n corresponding to the chemical potential shown in the legend of the upper panel.

10. Single site DMFT with $J_1 \neq 0$ and $J_2 \neq 0$

As the Hubbard model with no and one ancilla qubit per site have been explored, it is now time to include on the final qubit. Using the results of the previous chapter a chemical potential $\mu = 0.7$ is chosen at which the spectral function of the Kondo lattice is metallic. The other parameters are chosen as followed:

N_{keep}	Λ	T	U	J_1	J_2	μ	t	n_z
2000	2	1e-6	0	1	[0.1,10]	0.7	0.5	2

Table 10.1: Parameters for the single site DMFT calculations of the Zhang-Sachdev Hamiltonian. The parameters are defined as in Table 8.1 and 9.1.

As it can be seen the second ancilla spin has an immediate effect on the lattice (Fig. 10.1). The spectral function has a now peak at around $\omega = 0$, which shifts to $\omega \approx -0.7$ for $J_2 = 2$. For values greater than $J_2 = 3$ the changes to the peak are marginal and only the outskirts of the function are different. This is due to the fact that both ancilla spins go into a singlet state. The lattice electrons remain free and can hopp between different sites as there is no interaction U, thus the lattice is metallic.
Looking closer at the formation of the ancilla quibt singlet in the J_2 interval $[0.1, 1]$ (Fig. 10.1 lower panel and 10.2), one sees that for a small interaction J_2 a peak occurs at $\omega = 0$. Dialing up J_2 results in broadening of this peak while the other two peaks decrease and even vanish for a large enough J_2.
Now going over to the verification of Luttinger's theorem, the methods introduced in chapter 7 will be used to compare the filling after the theorem to the filling calculated by the DMFT.

J_2	0.1	0.2	0.3	0.4	0.5	0.6	0.7	0.8	0.9
DMFT	1.4473	1.5253	1.5788	1.6159	1.6424	1.6623	1.6779	1.6904	1.7005
Luttinger	1.4458	1.5242	1.5785	1.6156	1.6422	1.6623	1.6778	1.6904	1.7004

J_2	1	2	3	4	5	6	7	8	9	10
DMFT	1.7091	1.7534	1.7703	1.7798	1.7863	1.7894	1.7925	1.7949	1.7967	1.7981
Luttinger	1.7090	1.7533	1.7708	1.7803	1.7861	1.7902	1.7931	1.7954	1.7971	1.7986

Table 10.2: Comparison between the occupation of the lattice after the DMFT calculations and the theoretical filling after Luttinger's theorem.

As it can be seen Luttinger's theorem is fulfilled for all values of J_2 (Fig. 10.3). It should be noted that the filling extracted from to DMFT calculations doesn't take the two ancilla qubits into account and therefore, they must be added separately to the filling as above done. However, because the filling is defined in modulo 2 (chapter 7) this won't change the bare values of n.

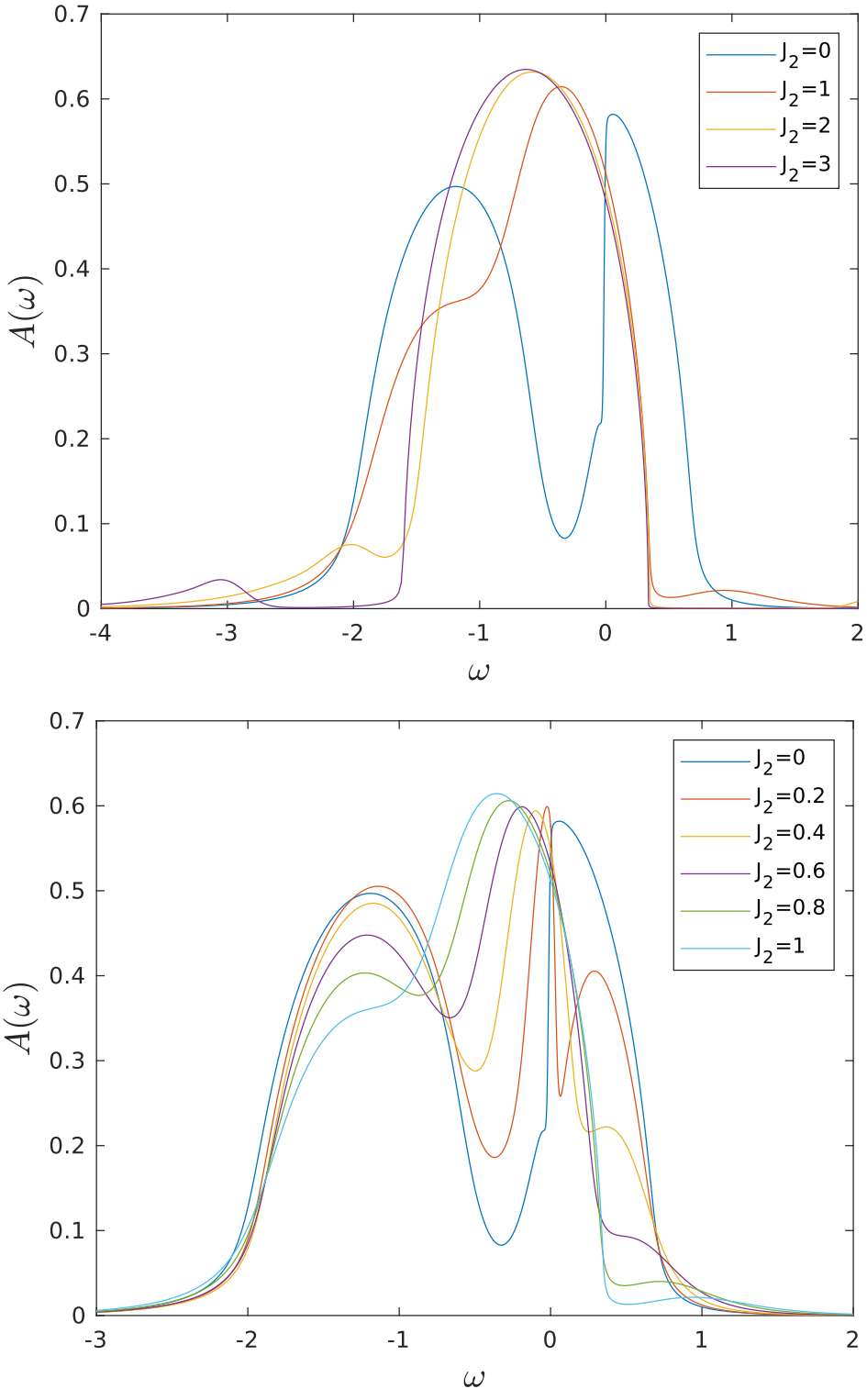

Figure 10.1: Spectral functions of the lattice model for J_2 variation. The upper panel shows them in an broader interval of $J_2 \in [0, 3]$, while the lower panel zooms in on $J_2 \in [0, 1]$

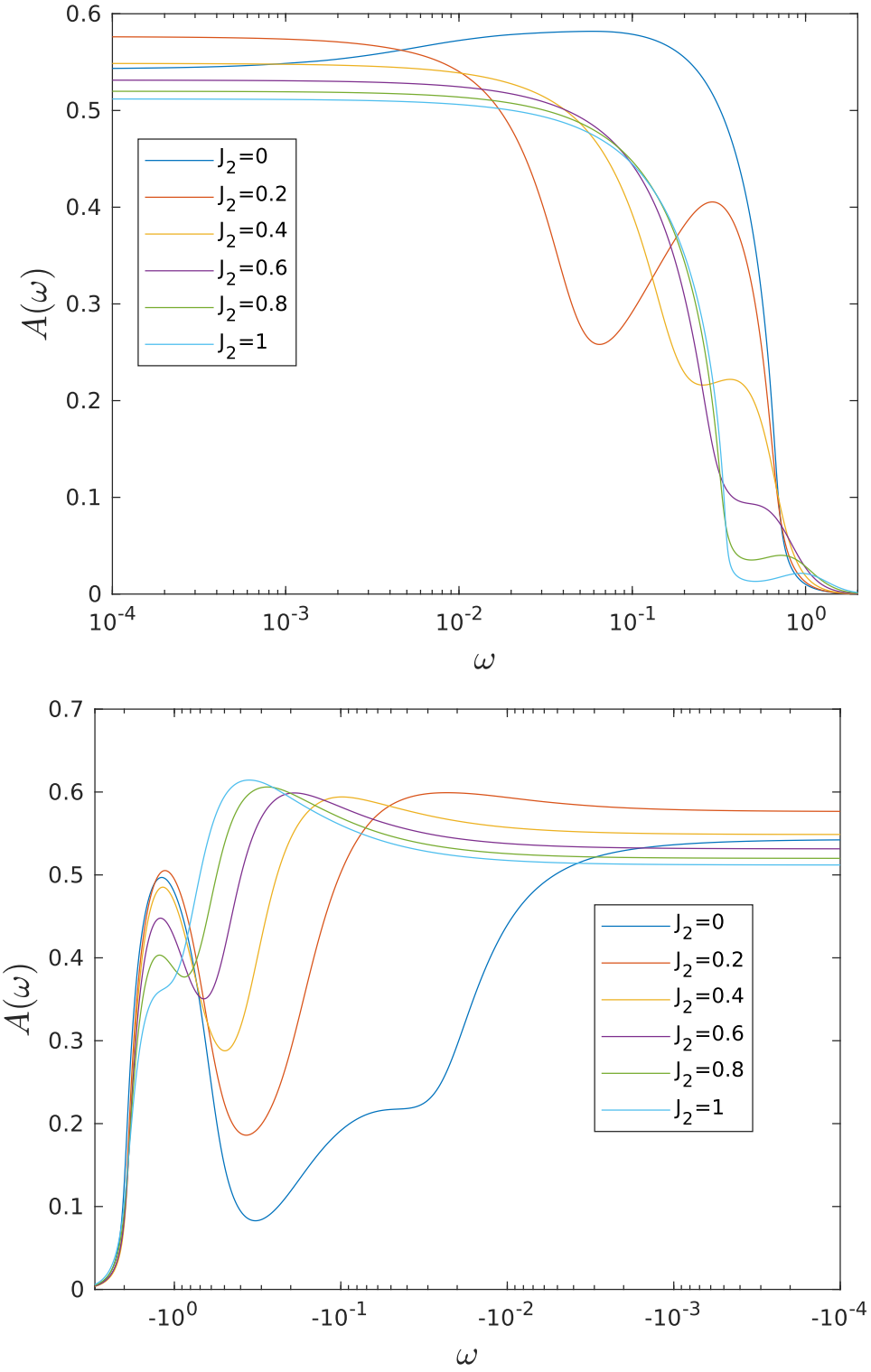

Figure 10.2: Spectral functions of the lattice model for J_2 variation on a logarithmic ω axis. The upper panel shows them in the interval $\omega \in [10^{-4}, 2]$, while the lower panel is in the interval $\omega \in [-3, -10^{-4}]$

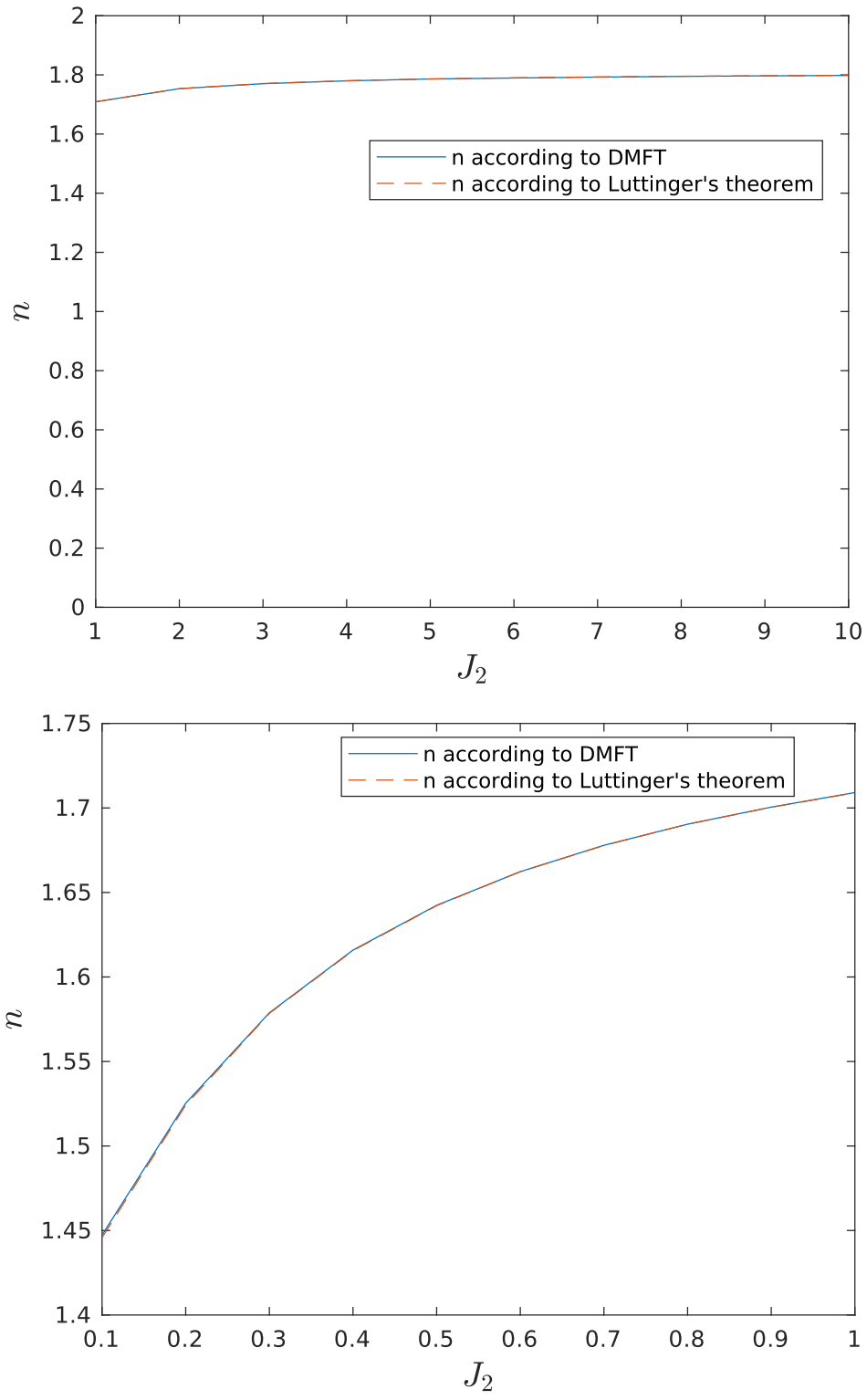

Figure 10.3: Verification of Luttinger's theorem versus the occupation n derived by the DMFT calculations. The upper panel shows the broader interval $J_2 \in [1, 10]$, while the lower panel zooms in on $J_2 \in [0.1, 1]$. As it can be seen there is no violation in either interval.

11. DCA with $J_1 = 0$

As the investigation of the Zhang-Sachdev-Hamiltonian with DMFT methods in the previous chapters have shown no interesting phase transitions or violations of Luttinger's theorem, one hopes to find more compelling results by examining short range non-local correlations via DCA calculations (chapter 3).
Starting with the analysis of the model, the interaction J_1 will be set again to 0. Like in chapter 8 this results again in a simple Hubbard model as J_1 couples the ancilla qubits with the lattice. Starting from half-filling the lattice will be hole doped. The remaining parameters are chosen as:

N_{keep}	Λ	T	U	J_1	J_2	n	μ	t	t'	n_z
5000	4	1e-5	2.5	0	50	[1.6,2]	1	1/4	-0.3/4	2

Table 11.1: Values for DCA calculations of the lattice model with $J_1 = 0$. Here t' is the next nearest neighbour hopping amplitude. The other parameters are defined as in Table 8.1 and 9.1.

As we are considering just a Hubbard model the resulting spectral functions should be comparable with the continuous-time quantum Monte Carlo (CTQMC) calculations of [7]. Starting from half-filling both patches are in an insulating phase with a gap at $\omega = 0$. Looking at the plus patch (Fig. 11.1 upper panel), hole doping results in a metallic phase. Further increasing the doping leads to spectral weight centered around $\omega = 0$.
The minus patch (Fig. 11.1 lower panel) however stays insulating at first, when the doping is increased. It develops a sharp peak at around $\omega = 0^+$, which grows and moves closer towards $\omega = 0$ for increased doping. At a doping level of $n < 1.7$ the minus patch becomes metallic as well. Overall, the results of the DCA calculations produce similar results as the CTQMC of [7].
As it has been seen, that for a doping $n \in [1.7, 2]$ the minus patch remains insulating while the plus patch becomes metallic, this area becomes of great interest as it is an indication for fermi arcs. Calculating the occupation after Luttinger's theorem and comparing them to results of the DCA calculations however, leads to:

n	1.9	1.8	1.7	1.6
DCA	0.9499	0.8997	0.8504	0.7999
Luttinger	0.9470	0.8942	0.8429	0.7964

Table 11.2: Comparison between the occupation of the lattice after the DCA calculations and the theoretical filling after Luttinger's theorem. The filling after Luttinger's theorem has been calculated without any interpolation methods.

As it can be seen both occupations are overall similar and there is no violation of Luttinger's theorem. It should be noted that $n = 2$ has been omitted from the comparison as both patches are insulating at this filling and therefore, won't show any Fermi surface whose volume could be calculated.

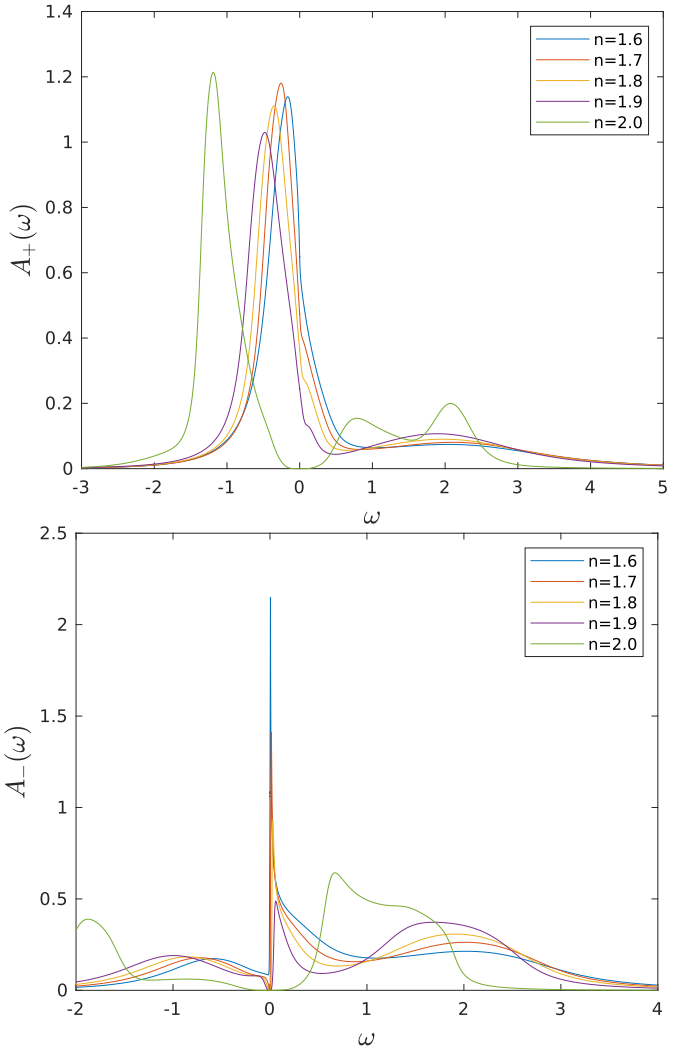

Figure 11.1: Spectral functions of the hole doped plus patch (upper panel) and minus patch (lower panel) at different fillings.

12. DCA with $J_2 = 0$

As we have discussed the Hubbard model with the DCA approach, now one ancilla spin will be added to the lattice resulting again into a Kondo lattice. This lattice will be first analyzed by changing the doping and afterwards by varying the interaction J_2. In both cases Luttinger's theorem will be calculated as well as the Fermi surfaces and the band structures in order to find a phase transition between regimes where Luttinger's theorem is violated and regimes where it is fulfilled.

12.1 Variation of the doping

Starting with the variation of the doping, the chemical potential will be varied in order to perform the necessary shifts of the doping. The parameters of the DCA calculations are chosen as followed:

N_{keep}	Λ	T	U	J_1	J_2	μ	t	t'	n_z
5000	4	1e-10	0	0.1	0	[-0.5,0.5]	1/4	-0.3/4	2

Table 12.1: Parameter for the variation of the Kondo lattice's doping. The parameters are defined as in Table 8.1, 9.1 and 11.1.

Looking at the spectral function of both patches it can be seen that a change in the chemical potential only leads to a shift of them. Additionally, a peak forms at $\omega = 0$ for a $\mu > -0.3$ (Fig. 12.1).

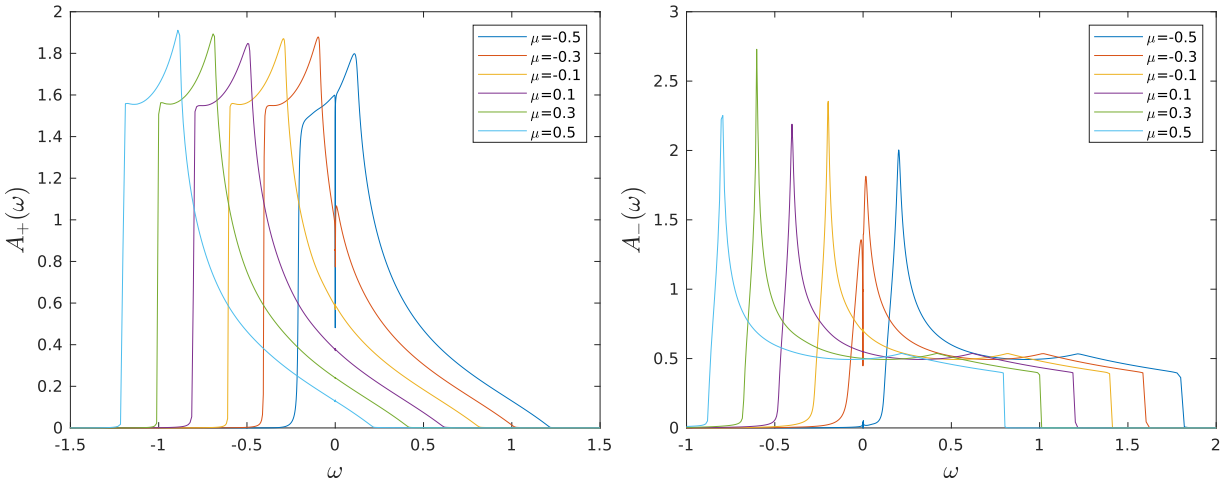

Figure 12.1: Spectral functions for the doped Kondo lattice. Both the plus patch (left panel) as well as the minus patch (right panel) feature a peak at $\omega = 0$ for $\mu < -0.3$.

Going over to Luttinger's theorem a clear violation can be seen:

μ	-0.5	-0.3	-0.2	-0.1	0	0.1	0.2	0.3	0.4	0.5
DCA +1	1.3227	1.7208	1.9411	2.0877	2.2049	2.3039	2.3911	2.4689	2.5398	2.6047
Luttinger	0.8235	0.7190	0.9400	1.0867	1.2039	1.3034	1.3906	1.4687	1.5396	1.6049

Table 12.2: Comparison between the occupation of the Kondo lattice after the DCA calculations and the theoretical filling after Luttinger's theorem for a variation of the chemical potential μ. The filling after Luttinger's theorem has been calculated without any interpolation methods.

The value of $\mu = -0.4$ has been omitted as the DCA calculations failed for this chemical potential. Furthermore, the ancilla spin has to be added separately to the DCA filling, in order to capture the whole lattice occupation. Therefore, some values of n are chosen larger than 2, in order to get a smooth plot of the values.
For values of $\mu > -0.3$ the theorem predicts one less particle than the lattice actually possesses. However, for $\mu = -0.5$ the differences between Luttinger's theorem and the lattice occupation goes down to half a particle (Fig. 12.2). This may be a result of the Rudermann-Kittel-Kasuya-Yosida (RKKY) interaction. This interaction stems from the long distance correlation between two local moments, here the ancilla qubits. They interact through the conduction electrons which get correlated/anticorrelated by the coupling between the bath and the ancilla qubits [9]. Wether this interaction is antiferromagnetic or ferromagnetic depends on the filling and the distance between the two local moments. In this case a transition from an antiferromagnetic to ferromagnetic RKKY interaction possibly has occurred when the chemical potential has been set to $\mu = -0.5$. This can be seen when looking at the renormalization group flows, which are not included in this thesis.

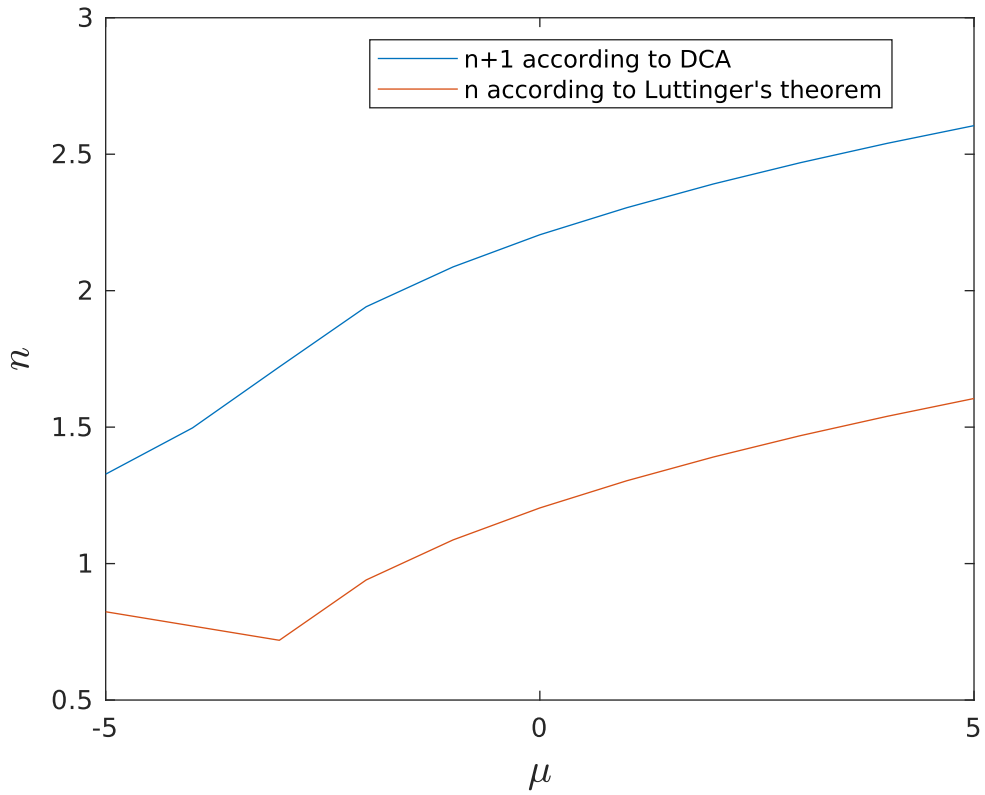

Figure 12.2: Verification of Luttinger's theorem at different values of μ versus the occupation derived by the DCA calculations. As it can be seen there is a clear violation for Luttinger's theorem as a particle is missing in the theorem's prediction in $\mu \in [-0.3, 0.5]$. At $\mu = -0.5$ the difference goes down to half a particle possibly because the RKKY interaction becomes ferromagnetic.

This transition can also be observed in the Femi surfaces and band structures. Starting from $\mu = 0.5$ the Fermi surface is relative small (Fig 12.3 lower panel) and starts growing for smaller values of μ reaching its maximum at $\mu = -0.3$ (Fig 12.3 middle panel). However, setting the chemical potential to $\mu = -0.5$ the Fermi surface decreases suddenly (Fig 12.3 upper panel).
The band structures will remain mostly the same for a variation of the chemical potential 12.4. Going from $\mu = 0.5$ downwards they shift upwards as a result of the decreasing chemical potential. Additionally, a horizontal peak develops at $\omega = 0$ when setting a negative potential.

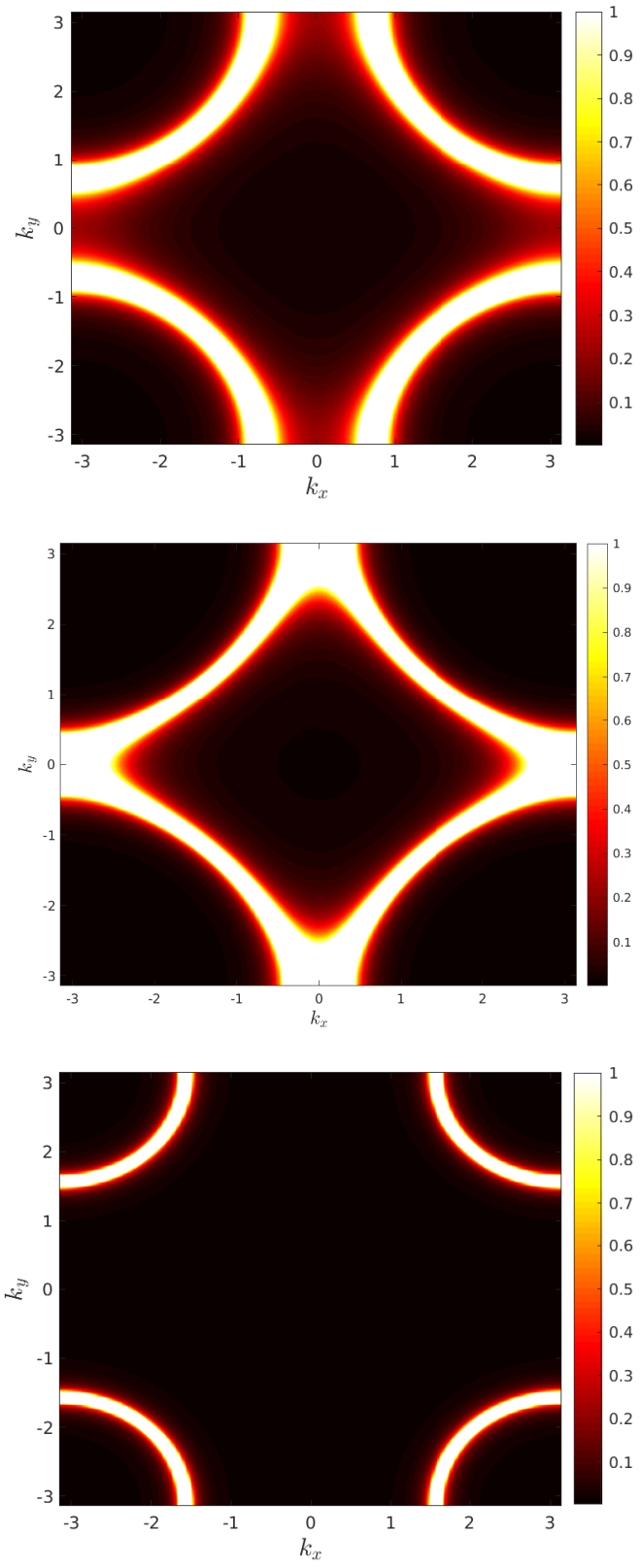

Figure 12.3: Fermi surfaces for $\mu = -0.5$ (upper panel), $\mu = -0.3$ (middle panel) and $\mu = 0.5$ (lower panel). M-interpolation has been used to extract the figures.

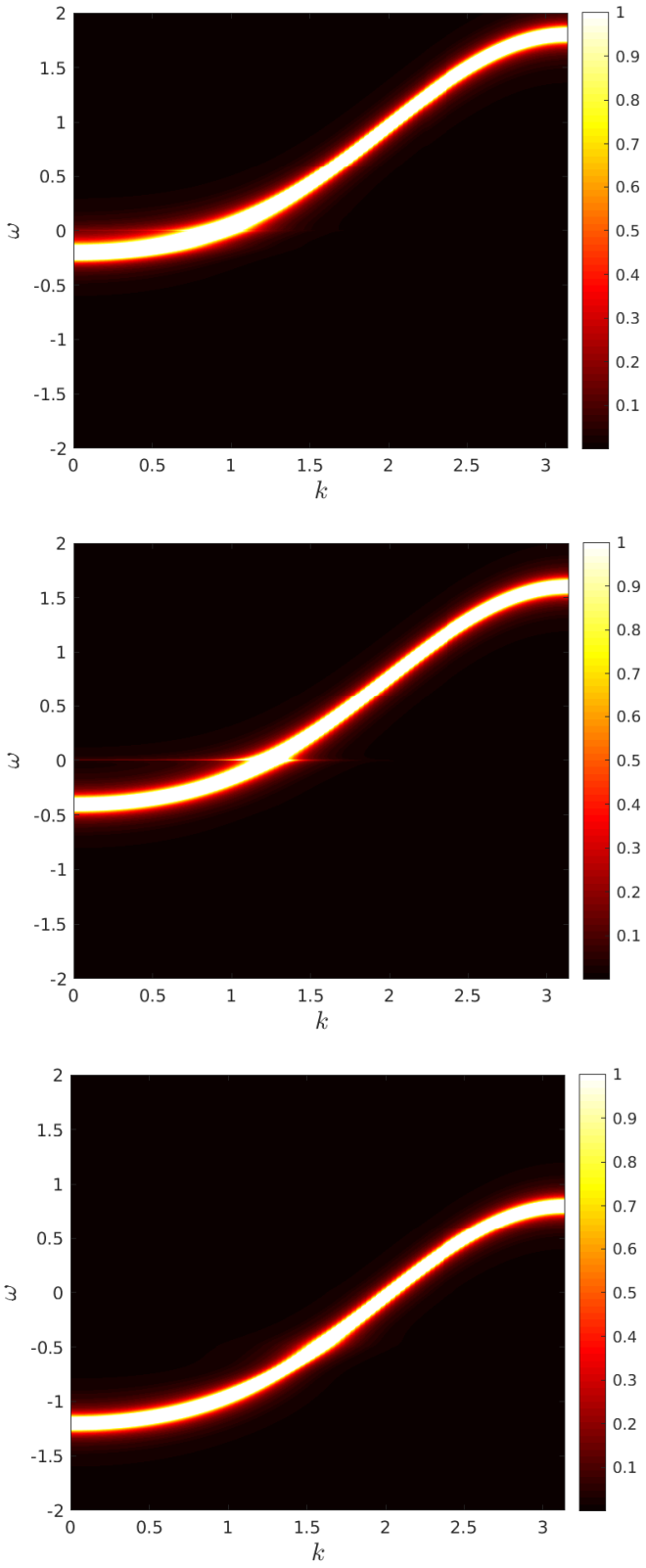

Figure 12.4: Band structures for $\mu = -0.5$ (upper panel), $\mu = -0.3$ (middle panel) and $\mu = 0.5$ (lower panel). M-interpolation has been used to extract the figures. The band structure follows the path from the (0,0) point in the Brillouin zone to the (π, π) point.

12.2 J_1 variation

As a clear violation of Luttinger's theorem has been found, a possible phase transition to an area where the theorem is fulfilled will be explored. To achieve this the chemical potential will be fixed while the interaction J_1 will be varied. The parameters are chosen as followed:

N_{keep}	Λ	T	U	J_1	J_2	μ	t	t'	n_z
5000	4	1e-10	0	[0.1,1]	0	-0.3	1/4	-0.3/4	2

Table 12.3: Parameters for the variation of J_1 in the Kondo lattice model. The parameters are defined as in Table 8.1, 9.1 and 11.1.

First, the spectral functions are analyzed (Fig. 12.5). Both patches start with a slight indentation at $\omega = 0$, but are still both metallic. The plus patch however, develops a gap at this position and becomes immediately insulating when setting $J_1 > 0.3$. The gap increases for bigger values of J_1. The minus patch on the other hand stays metallic even for different J_1. The indentation enlarges here while slightly moving away from $\omega = 0$.

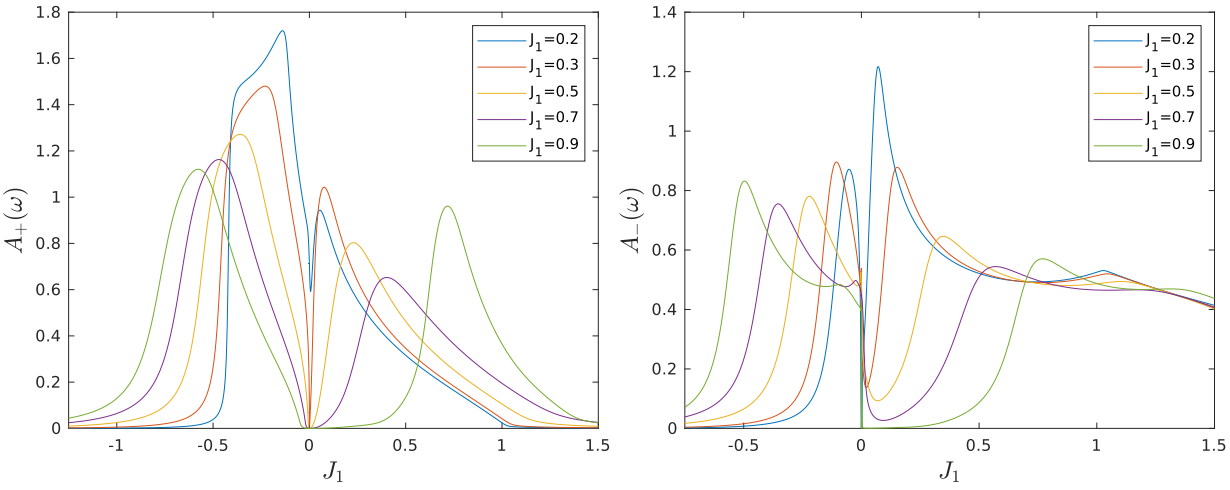

Figure 12.5: Spectral function of the J_1 varied Kondo lattice with the plus patch (right panel) and minus patch (left panel)

Moving on to Luttinger's theorem following values have been extracted:

J_1	0.1	0.2	0.3	0.4	0.5	0.6	0.7	0.8	0.9	1
DCA+1	1.7208	1.7373	1.7456	1.7716	1.8085	1.8508	1.8960	1.9421	1.9902	1.9976
Luttinger	0.7191	0.7440	1.7455	1.7710	1.8076	1.8473	1.8936	1.9427	1.9929	2.0

Table 12.4: Comparison between the occupation of the Kondo lattice after the DCA calculations and the theoretical filling after Luttinger's theorem for a variation of the interaction J_1. The filling after Luttinger's theorem has been calculated without any interpolation methods.

It can be seen (Fig. 12.6) that for the positive J_1 values up to $J_1 = 0.2$ the difference between the theoretical occupation calculated by Luttinger's theorem and the occupation derived from the DCA is exactly one particle. The theorem is violated in this area. However, for $J_1 > 0.2$ Luttinger's theorem is suddenly satisfied and this differences vanishes. It should be noted that again the ancilla spin has to be added separately to the lattice filling.

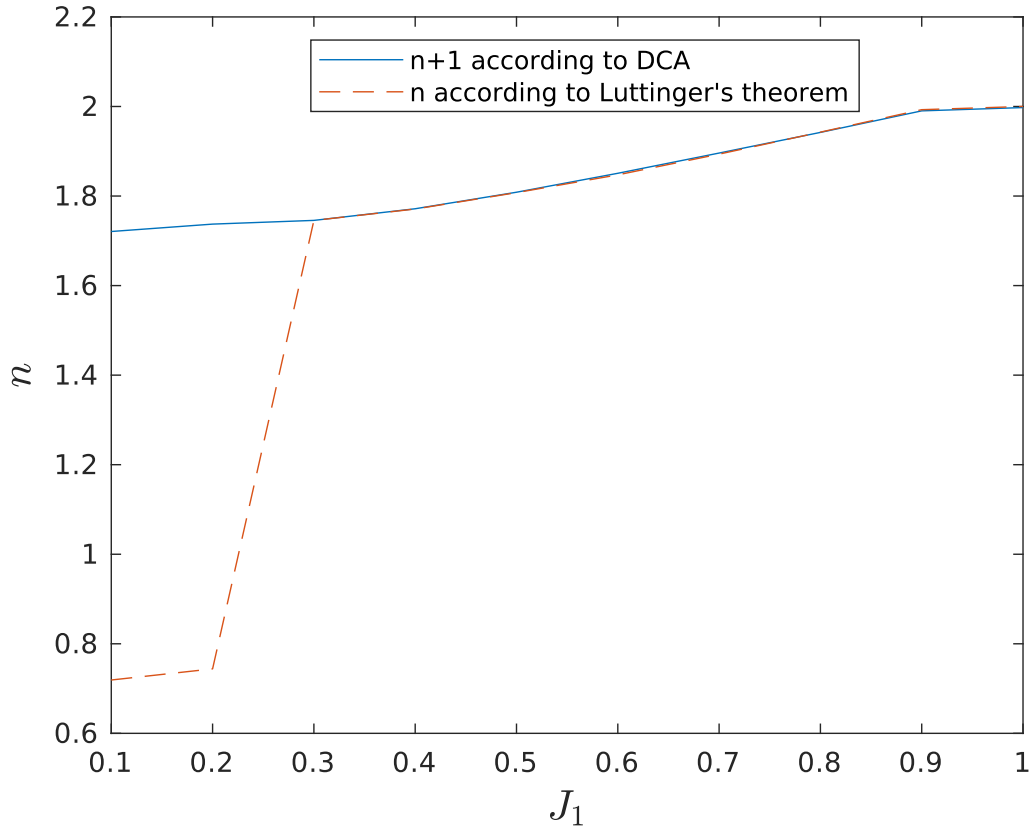

Figure 12.6: Verification of Luttinger's theorem at different values of J_1 versus the occupation derived by the DCA calculations.

This transition has also an immediate effect onto the Fermi surfaces. For the area where

Luttinger's theorem is broken the resulting Fermi surface is large and reaches deep into the Brillouin zone (Fig. 12.7 upper panel). Setting now $J_1 > 0.2$ the Fermi surface reduces, only covering the edges of the Brillouin zone (Fig. 12.7 lower panel). Increasing J_1 further decreases the Fermi volume even more.
The band structures experience also a change when going from $J_1 = 0.2$ to $J_1 = 0.3$. In the area of a broken Luttinger's theorem the band is continuous with a small, vertical peak at $\omega = 0$ (Fig. 12.8 upper panel). Increasing J_1 towards the critical point leads to a narrowing of the band at $\omega = 0$. Going over to the regime where the theorem is fulfilled, a gap develops in the band structure just slightly above $\omega = 0$ (Fig. 12.8 lower panel). For larger values of J_1 the gap becomes wider while still starting at $\omega > 0$.
Interestingly enough, if the filling is moved closer to half-filling, the critical point of the transition stays between $J_1 = 0.2$ and $J_1 = 0.3$, but the structure of the Fermi surfaces changes drastically (Fig. 12.9). Instead of a closed Fermi surface, Fermi arc like structure for $\mu = -0.2$ appear similar to the findings in [7].
The band structures for $\mu = -0.2$ and $J_1 = 0.2$ have even before the transition to an area where Luttinger's theorem is fulfilled a gap at $\omega > 0$ (Fig. 12.10 upper panel). This gap gets only larger for $J_1 = 0.3$ (Fig. 12.10 lower panel).

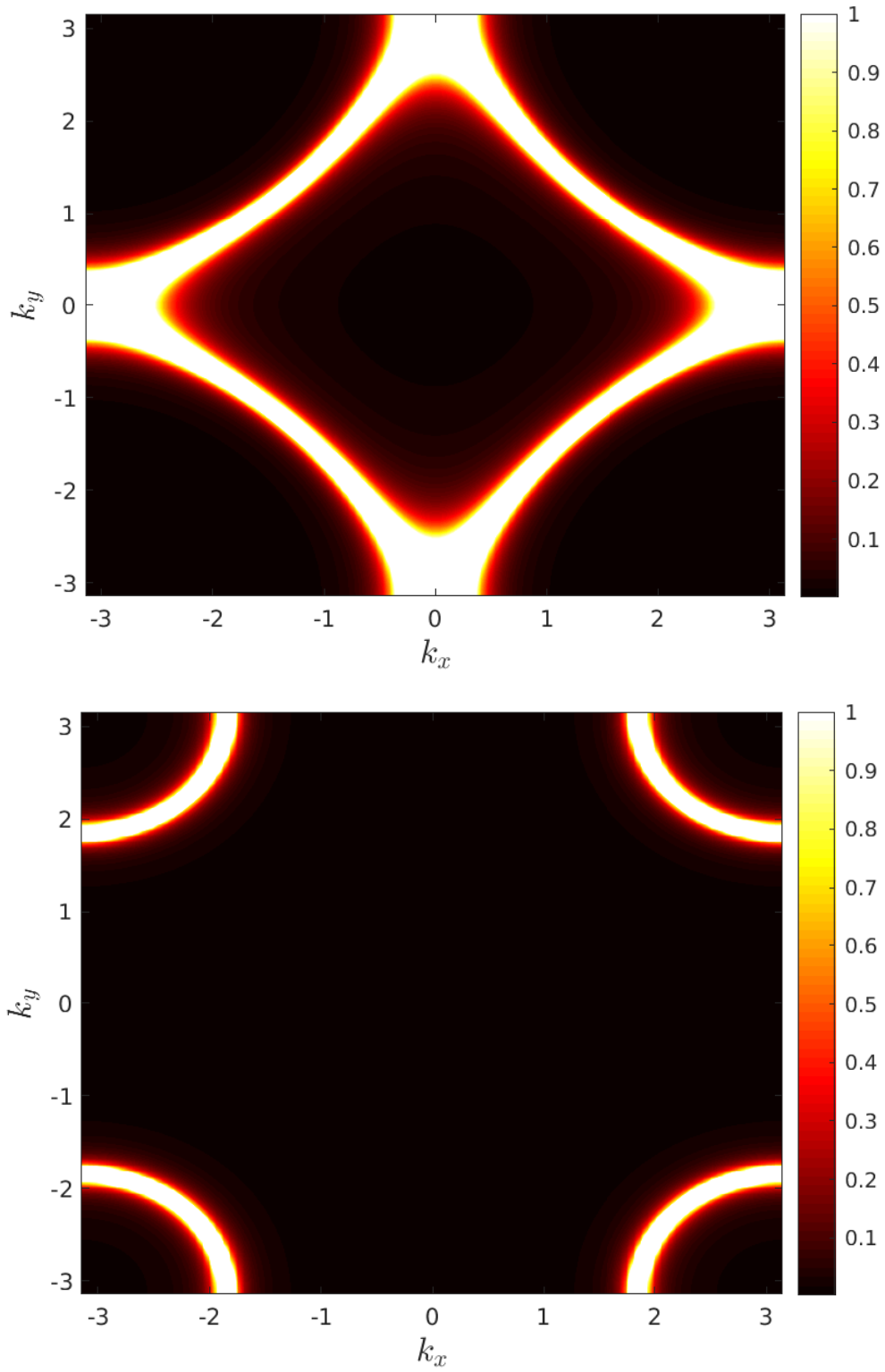

Figure 12.7: Fermi surfaces for $J_1 = 0.2$ (upper panel) and $J_1 = 0.3$ (lower panel) at $\mu = -0.3$. M-interpolation has been used to extract the figures.

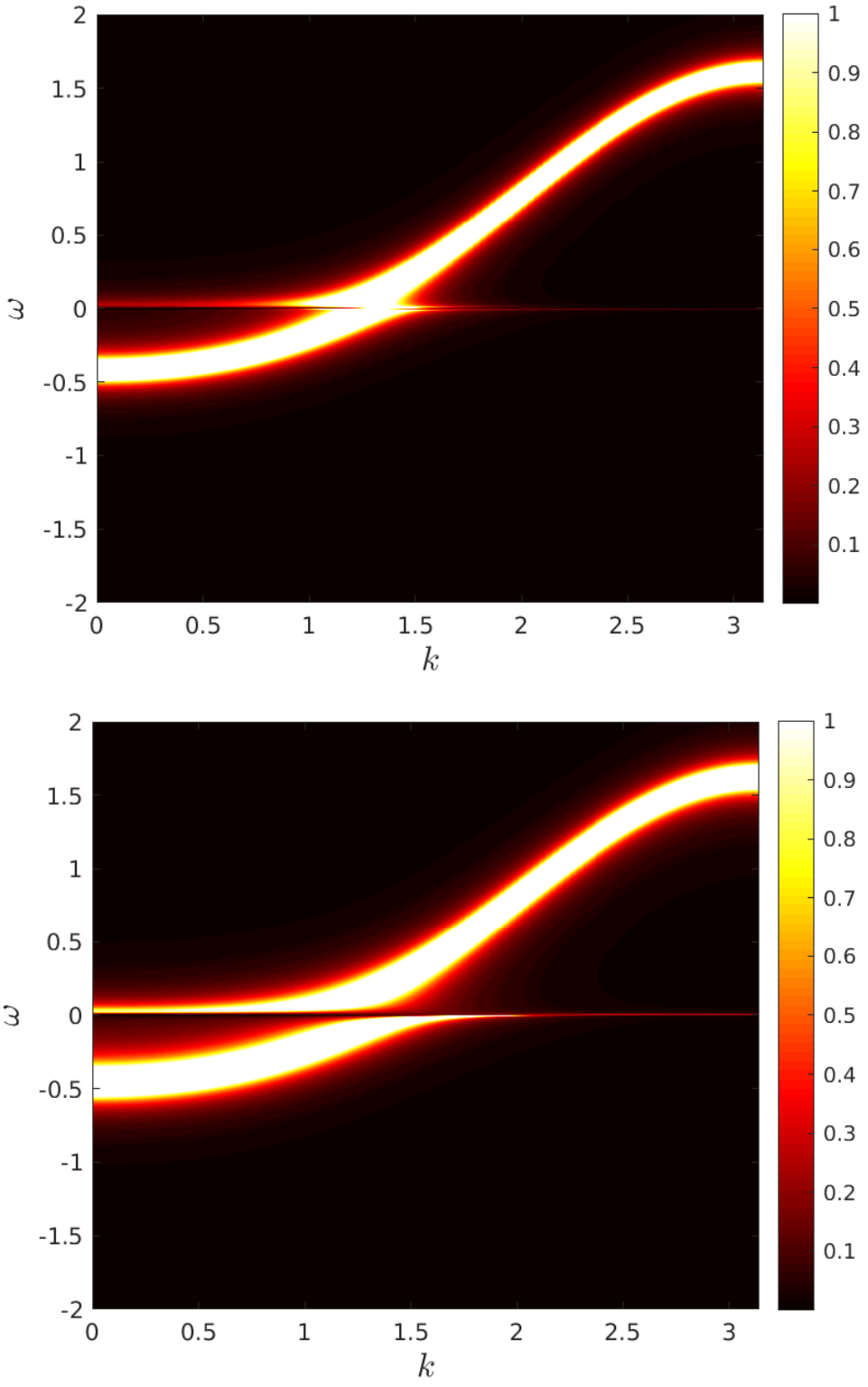

Figure 12.8: Band structures for $J_1 = 0.2$ (upper panel) and $J_1 = 0.3$ (lower panel) at $\mu = -0.3$. M-interpolation has been used to extract the figures. The band structure follows the path from the (0,0) point in the Brillouin zone to the (π, π) point.

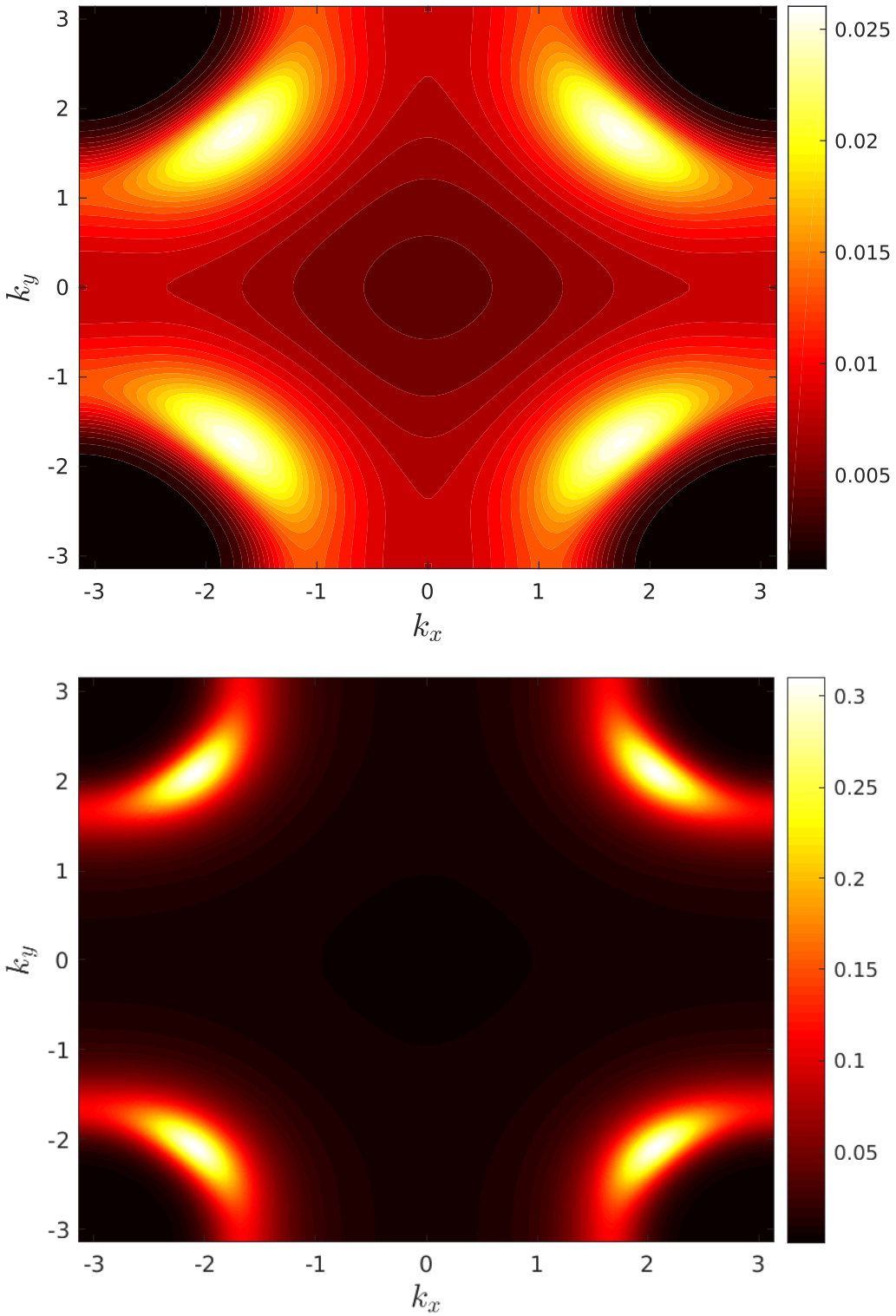

Figure 12.9: Fermi arc like structures for $J_1 = 0.2$ (upper panel) and $J_1 = 0.3$ (lower panel) at $\mu = -0.2$. M-interpolation has been used to extract the figures.

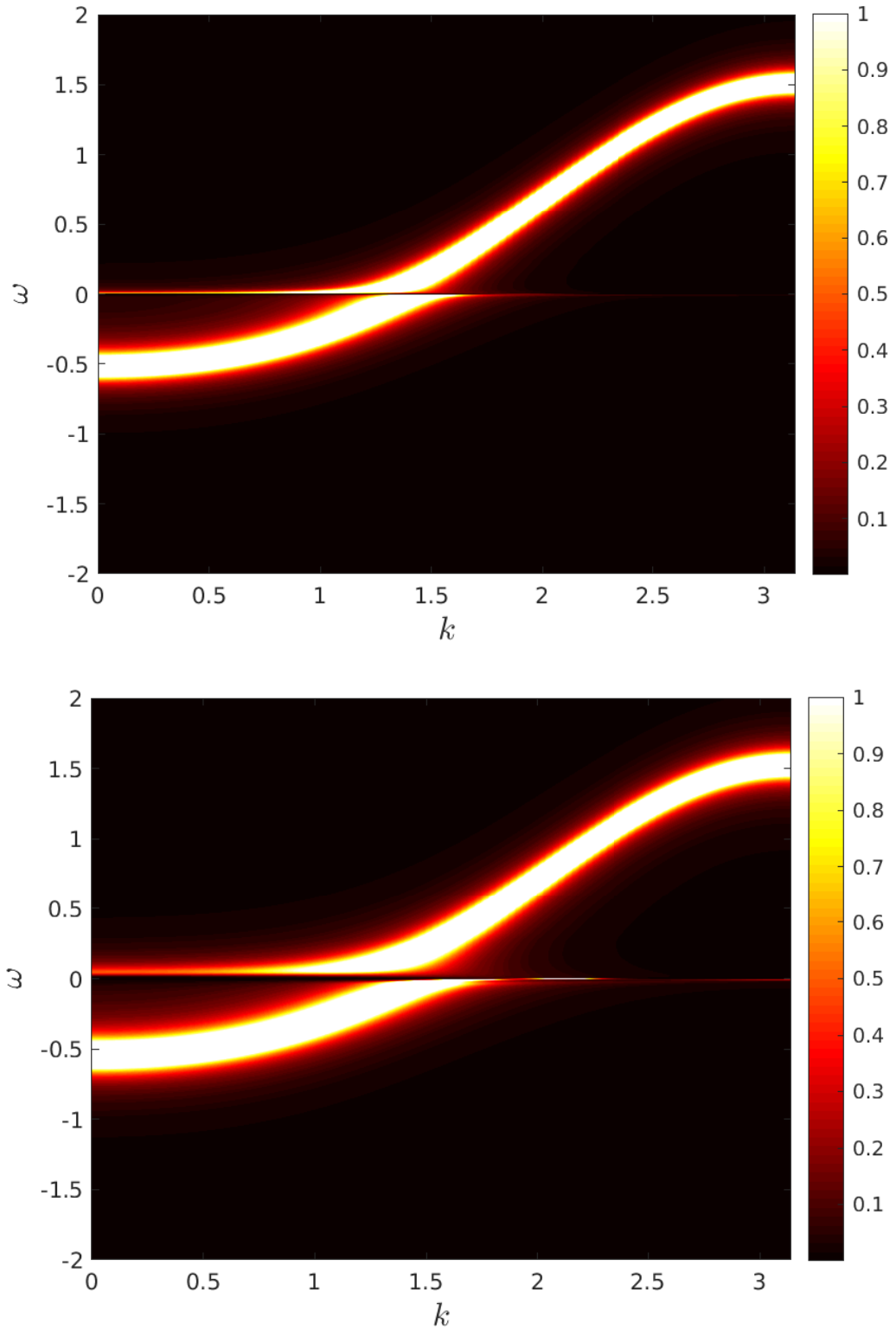

Figure 12.10: Band structures of the Fermi arc like structures for $J_1 = 0.2$ (upper panel) and $J_1 = 0.3$ (lower panel) at $\mu = -0.2$. M-interpolation has been used to extract the figures. The band structure follows the path from the (0,0) point in the Brillouin zone to the (π, π) point.

13. DCA with $J_1 \neq 0$ and $J_2 \neq 0$

In this last chapter the effects of two ancilla spins onto the lattice will be looked upon in the DCA calculations. J_2 will be varied while the other parameters remain fixed:

N_{keep}	Λ	T	U	J_1	J_2	μ	t	t'	n_z
5000	4	1e-10	0	1	[0,1]	-0.5	1/4	-0.3/4	2

Table 13.1: Parameters for the DCA calculations of the Zhang-Sachdev Hamiltonian. The parameters are defined as in Table 8.1, 9.1 and 11.1.

Looking first at the spectral functions again (Fig. 13.1), it can be seen that for $J_2 = 0$ the plus patch is insulating. For small values like $J_2 = 0.1$ a small peak develops at $\omega = 0$ and the patch becomes metallic. Increasing the interaction to $J_2 = 0.2$ leads to an immense growth of the peak at $\omega = 0$. Dialing up J_2 further results into a broadening of the peak. The minus patch in the other hand starts in a metallic state. Switching on J_2 to $J_2 = 0.1$ again a peak develops at $\omega = 0$ which grows drastically when the interaction is set to $J_2 = 0.2$. For bigger values of J_2 the peak moves away from $\omega = 0$ and decreases. At $J_2 = 1$ the patch is insulating due to the shift of the peak.

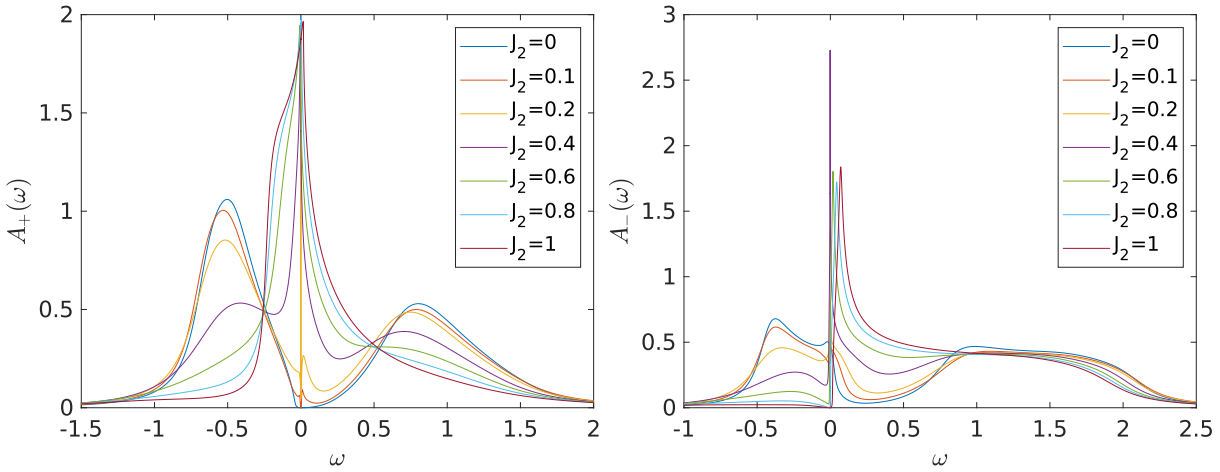

Figure 13.1: Spectral function of the J_2 varied Zhang-Sachdev lattice.

Looking at Luttinger's theorem following values of been extracted:

J_2	0.1	0.2	0.4	0.5	0.6	0.7	0.8	0.9	1
DCA	0.8174	0.7621	0.6582	0.6197	0.5826	0.5484	0.5211	0.5002	0.4843
Luttinger	1.3190	0.7567	0.6666	0.6060	0.5695	0.5413	0.5176	0.4980	0.4821

Table 13.2: Comparison between the occupation of the lattice model after the DCA calculations and the theoretical filling after Luttinger's theorem for a variation of the interaction J_2. The filling after Luttinger's theorem has been calculated without any interpolation methods.

To the occupation calculated by the DCA both ancilla qubits have to be added separately to capture the whole lattice filling. But, as the filling is defined in modulo 2 (chapter 7), this won't change the extracted values.
For $J_2 = 0.1$ a violation of Luttinger's theorem occurs as there is a difference of half a particle between the derived fillings (Fig. 13.2). This is probably again due to the switch into a ferromagnetic RKKY interaction. Going over to $J_2 = 0.2$ both calculated fillings match and therefore the theorem is satisfied.

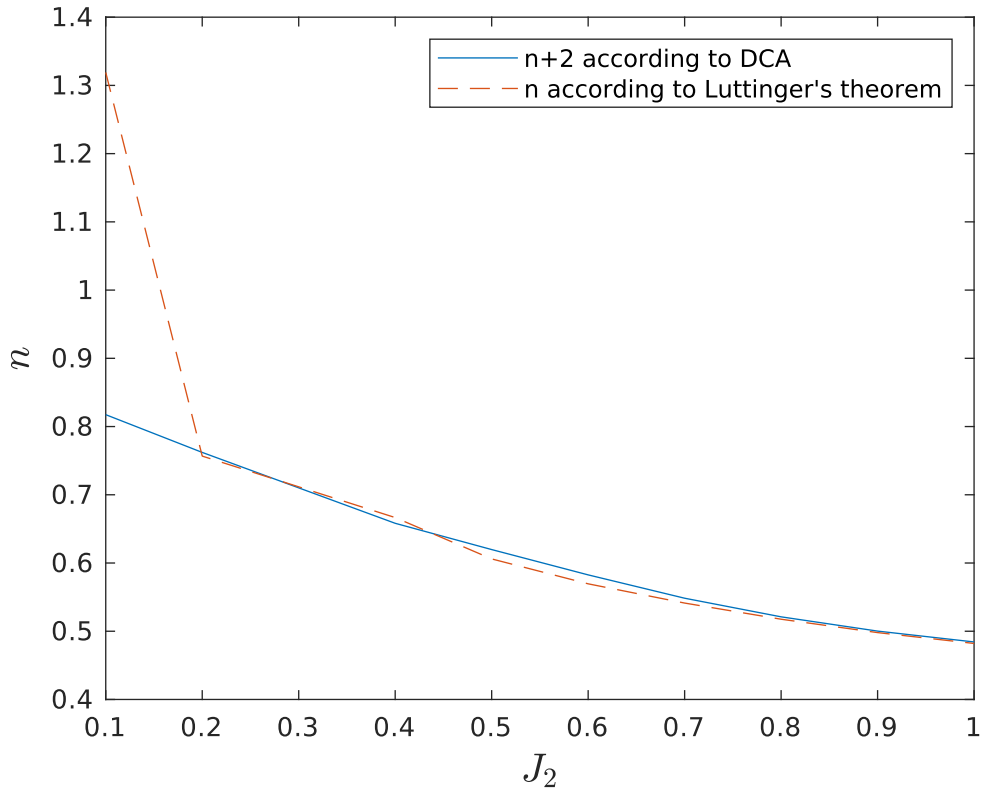

Figure 13.2: Verification of Luttinger's theorem at different values of J_2 versus the occupation derived by the DCA calculations.

This phase transition can also be observed in the Fermi surfaces of the lattice model. At $J_2 = 0.1$ the Fermi surface reaches far into the Brillouin zone, but has additionally a circle in the middle of the patch (Fig. 13.3 upper panel). Going over into the area where Luttinger's theorem is fulfilled at $J_2 = 0.2$ the Fermi surface grows larger and the circle disappears (Fig. 13.3 lower panel). For larger values of J_2 the Fermi surface will grow slightly larger.
The band structures experience also a change. At $J_2 = 0.1$ there are three distinctive bands. The first ancilla qubit has split the original band at $\omega > 0$ into a lower and upper band, while the second qubit splits the lower band at $\omega < 0$ (Fig. 13.4 upper panel). Because of this second split there is an additional circle in the Fermi surface. Setting $J_2 = 0.2$ will result into a slight increase of the gap between the middle band and the lower band (Fig. 13.4 lower panel).

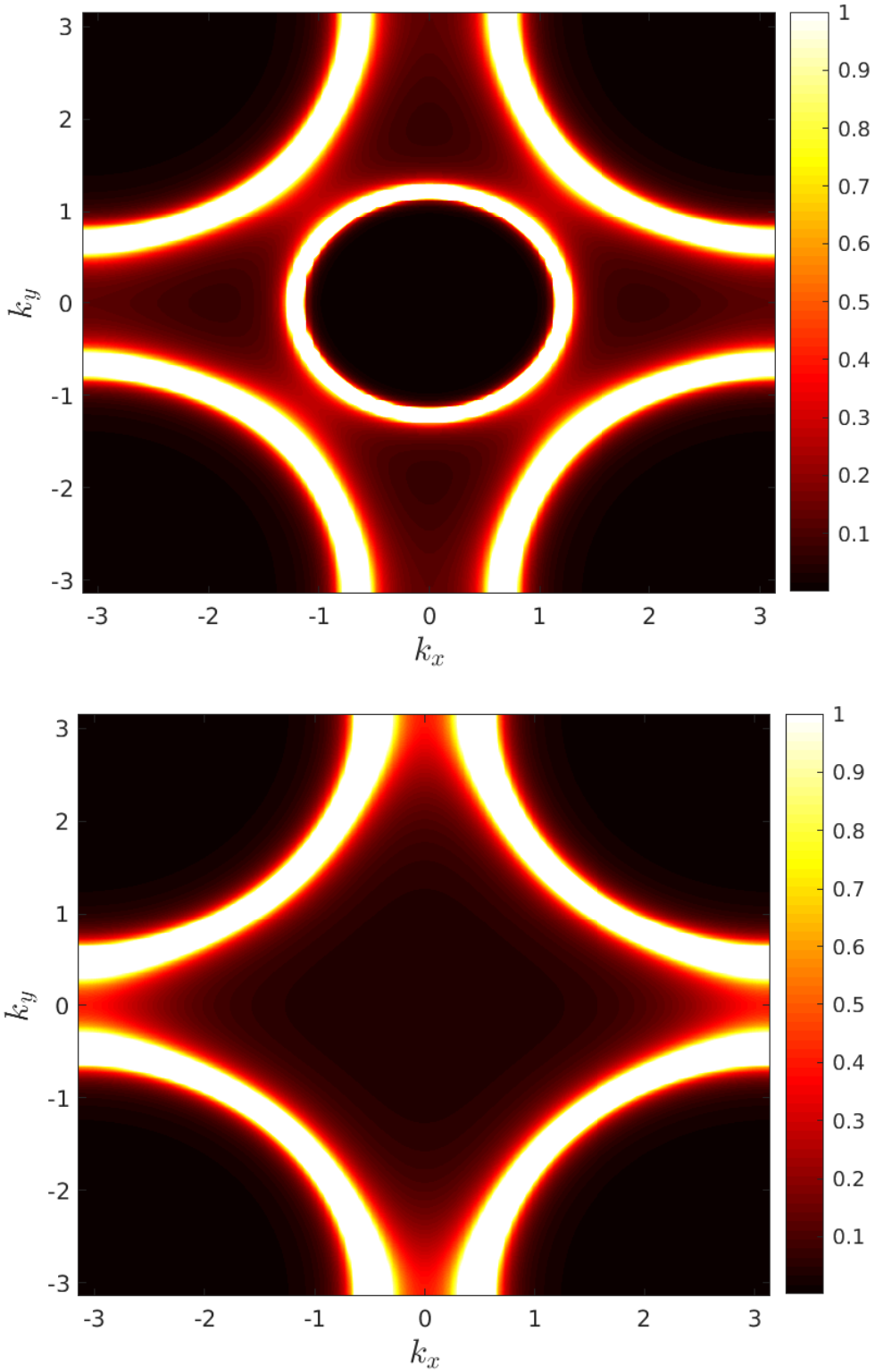

Figure 13.3: Fermi surfaces for $J_2 = 0.1$ (upper panel) and $J_2 = 0.2$ (lower panel). M-interpolation has been used to extract the figures.

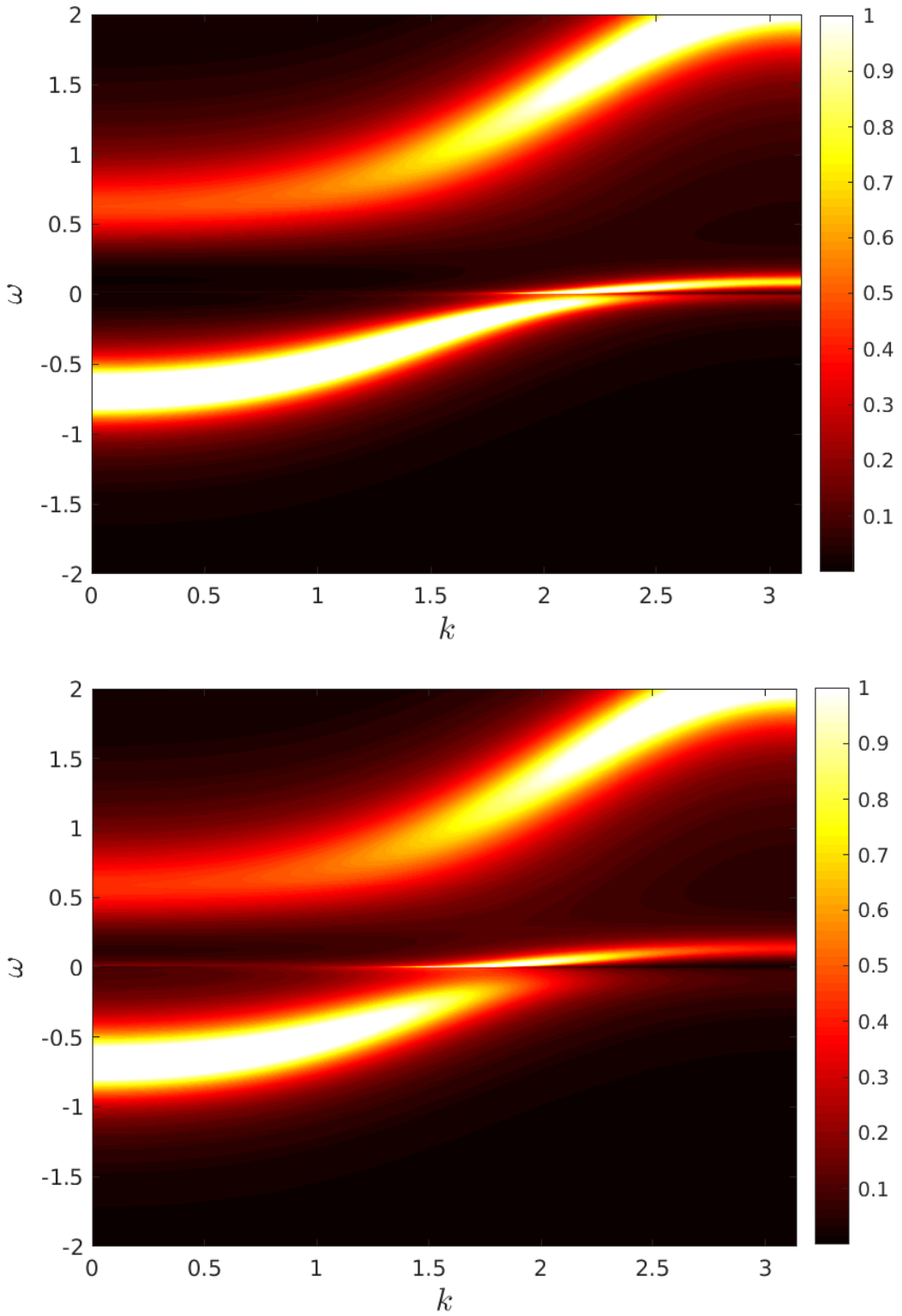

Figure 13.4: Band structures for $J_2 = 0.1$ (upper panel) and $J_2 = 0.2$ (lower panel). M-interpolation has been used to extract the figures. The band structure follows the path from the (0,0) point in the Brillouin zone to the (π, π) point.

14. Conclusion and Outlook

In this thesis, the effects of ancilla qubits onto the Hubbard model have been explored with great detail. Do to so dynamical mean field methods had been used with the numerical renormalization group acting as an impurity solver. Starting with the DMFT treatment of the Hubbard model the spectral functions at different Coulomb interactions U have been analyzed resulting into the well known metal-insulator transition at half filling.
Afterwards, an ancilla qubit per site has been added to the Hubbard model leading to the Kondo lattice. First, the interaction strength has been varied at half filling, but no phase transition could be found. Therefore, the filling has been varied at fixed values of J_1 resulting into a change of the insulating state into a metallic state.
Adding another ancilla qubit resulted into the Zhang-Sachdev lattice model [1]. As the starting point for the tuning of the interaction J_2 the chemical potential has been chosen so that the previous Kondo lattice was in a metallic phase. However, J_2 variation had shown that no phase transition exists in this calculations. Luttinger's theorem is also fulfilled for all values of J_2.
As the DMFT calculations produced no compelling results as well as no violations of Luttinger's theorem, the basic DMFT ideas have been expanded with the dynamical cluster approximation in order to incorporate short-ranged correlations. First, the Hubbard model was analyzed with the DCA. Comparing Luttinger's theorem with the calculated fillings showed no breaking of the theorem.
For the Kondo lattice however, a clear violation of Luttinger's theorem could be found. For both hole-doped as wells as particle-doped systems Luttinger's theorem predicted one less particle than the actual system possessed. Even more interesting, if the doping is further increased a presumable switch of the RKKY interaction to ferromagnetic probably occurred resulting in Luttinger's theorem predicting only half a particle less than expected. To find out possible phase transition between an area where Luttinger's theorem is violated to an area where it is satisfied, a hole-doped filing was choosen while J_1 was varied. Going from $J_1 = 0.2$ to $J_1 = 0.3$ this transition occurred and the Fermi surface decreased. Interestingly, if the chemical potential was set nearer towards half-filling, Fermi arc like structures appeared in the reconstruction of the Fermi surfaces.
Looking at the Zhang-Sachdev Hamiltonian within an DCA framework violations of Luttinger's theorem have been also found. Searching again for phase transitions J_2 had been varied with a hole-doped system. For $J_2 = 0.1$ the theorem was broken while a ferromagnetic RKKY interaction was supposedly present. Setting $J_2 = 0.2$ a phase transition

occurred and Luttinger's theorem was fulfilled. This was also visible in the Fermi surfaces were a transition took place between a Fermi surface with small volume to a Fermi surface with a large one.
Although, many calculations have ben done using both single site DMFT and DCA, there is still room for further inquires into the findings. While many violations of Luttinger's theorem could be found in the DCA calculations of the Kondo lattice and the Zhang-Sachdev Hamiltonian, the reason for them remains still unknown. Looking at the excitations could possibly lead to greater insight of this mechanism. Moreover, the reason for the switch of the RKKY interaction from antiferromagnetic to ferromagnetic needs to be investigated. Furthermore, greater tuning of the variables need to be done to get phase diagrams of the corresponding phase transitions.

A. Definitions and Notations

The definition of the retarded Green's function for fermionic operators A and B is

$$G^R_{AB}(t) = -i\Theta(t)\langle[A(t), B(0)]_+\rangle_T \tag{A.1}$$

with $\Theta(t)$ being the step-function, $[...]_+$ being the anticommutater and $\langle...\rangle_T$ being the thermal average in the grand canonical ensemble. As this thesis only uses retarded Green's function the index R will be dropped from G_{AB}.
The fermionic operator A and B are defined in the Heisenberg picture so the time evolution operator for $A(t)$ is :

$$A(t) = e^{\frac{i}{\hbar}Ht}Ae^{-\frac{i}{\hbar}Ht} \tag{A.2}$$

For the rest of this thesis all $\hbar$ will be set to 1. The equation of motion for an operator in the Heisenberg picture can be expressed as

$$\frac{dA(t)}{dt} = i[H, A(t)]_- \tag{A.3}$$

with $[...]_-$ being the commutation relations. With Eq.(A.3) used onto the Green's function, it reads:

$$\frac{d}{dt}G_{AB}(t) = -i\delta(t)\langle[A(0), B(0)]_+\rangle_T - \Theta(t)\langle[[A(t), H]_-, B(0)]_+\rangle_T \tag{A.4}$$

To solve this equation it is easier to evaluate it in frequency space., where the equation of motion becomes algebraic. Therefore we need to define the Fouriertransforms of the Green's function:

$$\begin{aligned} G_{AB}(\omega) &= \int_{-\infty}^{\infty} dt\ G_{AB}(t)\ e^{iwt} \\ G_{AB}(t) &= \int_{-\infty}^{\infty} \frac{dw}{2\pi}\ G_{AB}(\omega)\ e^{-iwt} \end{aligned} \tag{A.5}$$

Therefore, in frequency space the equation of motion becomes:

$$\omega G_{AB}(\omega) = \langle[A(0), B(0)]_+\rangle_T + G_{[A,H]_-,B}(\omega) \tag{A.6}$$

Furthermore, we need to express the spectral representation of the Green's function which is commonly defined as:

$$A_{AB}(\omega) = -\frac{1}{\pi}\mathrm{Im}(G_{AB}(\omega)) \tag{A.7}$$

As this thesis only describes fermions in the lattice model it is instructive to recapitulate the basic anticommutation relations for fermions:

$$[c_i, c_j^\dagger]_+ = \delta_{i,j} \quad [c_i, c_j]_+ = 0 \quad [c_i^\dagger, c_j^\dagger]_+ = 0 \tag{A.8}$$

For further discussion I refer to [21], [24], [22] and [23].

B. Derivation of the lattice Green's function

Here the lattice Greens's function will be completely derived. Starting with the lattice Hamiltonian in k-space (Eq. 2.9)

$$H_{\mathrm{latt,k}} = \underbrace{\sum_{k\in 1.BZ} (\varepsilon_k - \mu) c_k^\dagger c_k}_{H^0} + \sum_i H_i^{\mathrm{int}} \tag{B.1}$$

an equation of motion ansatz in frequency space (Eq. A.6) will be used to calculate the non-interacting Green's function:

$$\omega\ G^0_{\mathrm{latt,k}}(\omega) = \langle [c_k, c_k^\dagger]_+ \rangle_T + G^0_{[c_k, H^0]_-, c_k^\dagger} \tag{B.2}$$

The term $\langle [c_k, c_k^\dagger]_+ \rangle_T = \langle 1 \rangle_T = 1$ can be easily seen by following the anticommutation relations of fermions (Eq. A.8). Now only the term for $G^0_{[c_k, H^0]_-, c_k^\dagger}$ needs to be solved starting with the commutator $[c_k, H^0]_-$:

$$[c_k, H^0]_- = \sum_{\tilde{k}} (\varepsilon_{\tilde{k}} - \mu)[c_k, c_{\tilde{k}}^\dagger c_{\tilde{k}}] \tag{B.3}$$

By inserting

$$\begin{aligned} [c_k, c_{\tilde{k}}^\dagger c_{\tilde{k}}]_- &= c_k c_{\tilde{k}}^\dagger c_{\tilde{k}} - c_{\tilde{k}}^\dagger c_{\tilde{k}} c_k \\ &= c_k c_{\tilde{k}}^\dagger c_{\tilde{k}} - c_{\tilde{k}}^\dagger c_{\tilde{k}} c_k + c_{\tilde{k}}^\dagger c_k c_{\tilde{k}} - c_{\tilde{k}}^\dagger c_k c_{\tilde{k}} \\ &= [c_{\tilde{k}}^\dagger, c_k]_+ c_{\tilde{k}} + c_{\tilde{k}}^\dagger [c_{\tilde{k}}, c_k]_+ = \delta_{k,\tilde{k}} c_k \end{aligned} \tag{B.4}$$

into Eq. B.3 we get

$$[c_k, H^0]_- = (\varepsilon_{\tilde{k}} - \mu)\delta_{k,\tilde{k}} c_k = (\varepsilon_k - \mu) c_k \tag{B.5}$$

This result will be used to solve Eq. B.2:

$$\begin{aligned} \omega\ G^0_{\mathrm{latt,k}}(\omega) = \langle [c_k, c_k^\dagger]_+ \rangle_T + G^0_{[c_k, H^0]_-, c_k^\dagger} &= 1 + (\varepsilon_k - \mu) G^0_{\mathrm{latt,k}}(\omega) \\ \Leftrightarrow (\omega - \varepsilon_k + \mu) &= G^0_{\mathrm{latt,k}}(\omega)^{-1} \end{aligned} \tag{B.6}$$

Now that the non-interacting Green's function has been calculated, it can be inserted into the Dyson equation

$$G_{\mathrm{latt,k}}(\omega)^{-1} = G^{0}_{\mathrm{latt,k}}(\omega)^{-1} - \Sigma_k(\omega) \tag{B.7}$$

to get the interacting lattice Green's functions:

$$\begin{aligned} G_{\mathrm{latt,k}}(\omega)^{-1} &= \omega - \varepsilon_k + \mu - \Sigma_k(\omega) \\ \Leftrightarrow G_{\mathrm{latt,k}}(\omega) &= \frac{1}{\omega - \varepsilon_k + \mu - \Sigma_k(\omega)} \end{aligned} \tag{B.8}$$

C. Derivation of the impurity Green's function

In this Appendix the impurity Green's function will be derived. Starting with the Eq. 2.15-2.18

$$H_{\mathrm{im}} = H_{\mathrm{imp}} + H_{\mathrm{bath}} + H_{\mathrm{hyb}}, \tag{C.1}$$

$$H_{\mathrm{imp}} = (\varepsilon_d - \mu) d^\dagger d + H_{\mathrm{int}}, \tag{C.2}$$

$$H_{\mathrm{bath}} = \sum_{k\sigma} \varepsilon_k c^\dagger_{k\sigma} c_{k\sigma}, \tag{C.3}$$

$$H_{\mathrm{hyb}} = \sum_{k\sigma} V_k (d^\dagger c_{k\sigma} + h.c.) \tag{C.4}$$

an equation of motion ansatz in frequency space is used to derive the non-interacting Green's function $G_{\mathrm{im}}(\omega)$:

$$\omega G^0_{\mathrm{im}}(\omega) = \langle [d, d^\dagger]_+ \rangle_T - G^0_{[d_k, H^0_{\mathrm{im}}]_-, d^\dagger_k} \tag{C.5}$$

The term $\langle [d, d^\dagger]_+ \rangle_T = 1$ can be easily seen from the basic fermionic anticommutation relations (Eq. A8). Inserting Eq. B1 into the remaining term yields

$$G^0_{[d_k, H^0_{\mathrm{im}}]_-, d^\dagger_k} = G^0_{[d_k, H^0_{\mathrm{imp}}]_-, d^\dagger_k} + G^0_{[d_k, H_{\mathrm{bath}}]_-, d^\dagger_k} + G^0_{[d_k, H_{\mathrm{hyb}}]_-, d^\dagger_k} \tag{C.6}$$

To solve the individual part of Eq C.6 the following commutation relations will be needed:

$$[d, d^\dagger d]_- = [d, d^\dagger]_+ d - d^\dagger [d, d]_+ = d \tag{C.7}$$

$$[d, c^\dagger_{k\sigma} c_{k\sigma}]_- = [d, c^\dagger_{k\sigma}]_+ c - c^\dagger_{k\sigma} [d, c_{k\sigma}]_+ = 0 \tag{C.8}$$

$$[d, c^\dagger_{k\sigma} d]_- = [d, c^\dagger_{k\sigma}]_+ d - d^\dagger [d, d]_+ = 0 \tag{C.9}$$

$$[d, d^\dagger c_{k\sigma}]_- = [d, d^\dagger]_+ c_{k\sigma} - d^\dagger [d, c_{k\sigma}]_+ = c_{k\sigma} \tag{C.10}$$

with this expressions the terms of Eq. C6 can be calculated separately:

$$\begin{aligned} G^0_{[d_k,H^0_{\mathrm{imp}}]_-,d_k^\dagger} &= (\varepsilon_d-\mu)\langle\langle[d,d^\dagger d]_-,d^\dagger\rangle\rangle_w \overset{Eq.C.7}{=} \\ &= (\varepsilon_d-\mu)\langle\langle d,d^\dagger\rangle\rangle_w = (\varepsilon_d-\mu)G^0_{\mathrm{im}} \end{aligned} \tag{C.11}$$

$$G^0_{[d_k,H_{\mathrm{bath}}]_-,d_k^\dagger} = \varepsilon_k\langle\langle[d,c^\dagger_{k\sigma}c_{k\sigma}]_-\rangle\rangle_w \overset{Eq.C.8}{=} 0 \tag{C.12}$$

$$\begin{aligned} G^0_{[d_k,H_{\mathrm{hyb}}]_-,d_k^\dagger} &= \sum_{k\sigma}\Big(\langle\langle[d,d^\dagger c_{k\sigma}]_-,d^\dagger\rangle\rangle_w + \langle\langle[d,c^\dagger_{k\sigma}d]_-,d^\dagger\rangle\rangle_w\Big) \overset{Eq.C.9}{\underset{Eq.C.10}{=}} \\ &= \sum_{k\sigma} V_k\ G^0_{c_{k\sigma}d^\dagger} \end{aligned} \tag{C.13}$$

To solve the Green's function $G^0_{c_{k\sigma}d^\dagger}$ in Eq. C.13 another equation of motion ansatz is used:

$$\omega G^0_{c_{k\sigma}d^\dagger} = \langle[c_{k\sigma},d^\dagger]_+\rangle_T + G^0_{[c_{k\sigma},H_{\mathrm{im}}]_-,d^\dagger} = G^0_{[c_k,H_{\mathrm{im}}]_-,d^\dagger} \tag{C.14}$$

First the commutator $[c_{k\sigma},H_{\mathrm{im}}]_-$ will be expressed as

$$[c_{k\sigma},H_{\mathrm{im}}]_- = [c_{k\sigma},H^0_{\mathrm{imp}}]_- + [c_{k\sigma},H_{\mathrm{bath}}]_- + [c_{k\sigma},H_{\mathrm{hyb}}]_- \tag{C.15}$$

Each term will be considered separately:

$$[c_{k\sigma},H^0_{\mathrm{imp}}]_- = (\varepsilon_d-\mu)[c_{k\sigma},d^\dagger d] \overset{Eq.C.4}{=} 0 \tag{C.16}$$

$$[c_{k\sigma},H_{\mathrm{bath}}]_- = \sum_{k\sigma}\varepsilon_k[c_{k\sigma},c^{\dagger c_{\tilde{k}\sigma}}_{\tilde{k}\sigma}]_- \overset{Eq.B.4}{=} \varepsilon_k\ c_{k\sigma} \tag{C.17}$$

$$[c_{k\sigma},H_{\mathrm{hyb}}]_- = \sum_{k\sigma}\Big([d,c^\dagger_{k\sigma}c_{k\sigma}]_- + [d,c^\dagger_{k\sigma}d]_-\Big) \overset{Eq.C.9}{\underset{Eq.C.10}{=}} V_k\ d \tag{C.18}$$

Inserting the found expressions back into Eq. C.14

$$\begin{aligned} \omega G^0_{c_{k\sigma}d^\dagger}(\omega) &= \varepsilon_k G^0_{c_{k\sigma}d^\dagger} + V_k G^0_{\mathrm{im}} \\ G^0_{c_{k\sigma}d^\dagger} &= \frac{V_k}{\omega-\varepsilon_k}G^0_{\mathrm{im}} \end{aligned} \tag{C.19}$$

Now this term can be inserted back into Eq. C.13

$$G^0_{[d_k,H_{\mathrm{hyb}}]_-,d_k^\dagger} = \sum_k \frac{V_k^2}{\omega-\varepsilon_k}G^0_{\mathrm{im}} \tag{C.20}$$

so the non-interacting Green's function can be fully calculated with Eq. C.2, Eq. C.11, Eq. C.12 and Eq. C.20

$$\begin{aligned} \omega G^0_{\mathrm{im}}(\omega) &= 1 + (\varepsilon_d-\mu)G^0_{\mathrm{im}} + 0 + \sum_k \frac{V_k^2}{\omega-\varepsilon_k}G^0_{\mathrm{im}} \\ G^0_{\mathrm{im}}(\omega)^{-1} &= \omega - \varepsilon_d + \mu - \sum_k \frac{V_k^2}{\omega-\varepsilon_k} \end{aligned} \tag{C.21}$$

With the Dyson equation

$$G_{\mathrm{im}}(\omega)^{-1} = G^0_{\mathrm{im}}(\omega)^{-1} - \Sigma_{\mathrm{im}}(\omega) \tag{C.22}$$

the interacting impurity Green's function can be derived

$$\begin{aligned} G_{\mathrm{im}}(\omega) &= \frac{1}{\omega - \varepsilon_d + \mu - \sum_k \frac{V_k^2}{\omega - \varepsilon_k} - \sum_{\mathrm{im}}(\omega)} \\ G_{\mathrm{im}}(\omega) &= \frac{1}{\omega - \varepsilon_d + \mu - \Delta(\omega) - \sum_{\mathrm{im}}(\omega)} \end{aligned} \tag{C.23}$$

with $\Delta(\omega)$ being the hybridization function defined as

$$\Delta(\omega) = \sum_k \frac{V_k^2}{\omega - \varepsilon_k} \tag{C.24}$$

Bibliography

[1] Ya-Hui Zhang, Subir Sachdev. *From the pseudogap metal to the Fermi liquid using ancilla qubits*. Physical Review Reearch 2, 023172 (2020).

[2] Masaki Oshikawa. *Topological Approach to Luttinger's Theorem and the Fermi Surface of a Kondo Lattice*. Phys. Rev. Lett. 84, 3370 – Published 10 April 2000.

[3] Walter Metzner, Dieter Vollhardt, *Correlated lattice fermions in $d = \infty$ dimensions*. Phys. Rev. Lett., 62:324–327, Jan 1989.

[4] Antoine Georges, Gabriel Kotliar. *Hubbard model in infinite dimensions*. Phys. Rev. B, 45:6479–6483, Mar 1992.

[5] D. Vollhardt, K. Byczuk, M. Kollar. *Dynamical mean-field theory*. arXiv:1109.4833, 2011

[6] J. M. Luttinger. *Fermi Surface and Some Simple Equilibrium Properties of a System of Interacting Fermions*. Phys. Rev. 119.4 (1960), pp. 1153–1163.

[7] Michel Ferrero et al. *Pseudogap opening and formation of Fermi arcs as an orbital-selective Mott transition in momentum space*. Phys. Rev. B 80.6 (2009), p. 064501.

[8] Thomas Maier et al. *Quantum cluster theories*. Rev. Mod. Phys. 77.3 (2005), pp. 1027–1080.

[9] Andreas Gleis. *Cluster Dynamical Mean-Field + Numerical Renormalization Group Approach to Strongly Correlated Systems*. Master's thesis, Ludwig-Maximilians-Universität München, 2019.

[10] S. Badoux, W. Tabis, F. Laliberté et al. *Change of carrier density at the pseudogap critical point of a cuprate superconductor*. Nature 531, 210–214 (2016).

[11] S. Paschen, T. Lühmann, S. Wirth et al. *Hall-effect evolution across a heavy-fermion quantum critical point*. Nature 432, 881–885 (2004).

[12] A. Damascelli et al. *Angle-resolved photoemission studies of the cuprate superconductors*. Reviews of Modern Physics 75 (2003): 473-541.

[13] Katherina Stadler. *Towards exploiting non-abelian symmetries in the dynami- cal mean-field theory using the numerical renormalization group*. Master's thesis, Ludwigs-Maximilians-Universität München, 2013.

[14] Kenneth G. Wilson. *The renormalization group: Critical phenomena and the kondo problem*. Rev. Mod. Phys., 47:773–840, 1975.

[15] R. Bulla, T. A. Costi, and T. Pruschke. *Numerical renormalization group method for quantum impurity systems*. Rev. Mod. Phys., 80:395–450, 2008.

[16] Andreas Gleis. *On using the interleaved Numerical Renormalization Group as an impurity solver for the Dynamical Mean Field Theory*. Bachlor's thesis, Ludwig-Maximilians-Universität München, 2016.

[17] C. Lanczos. *An iteration method for the solution of the eigenvalue problem of linear differential and integral operators*. J. Res. Nat'l Bur. Std. 45, 1950.

[18] J. von Delft. `https://www.physik.uni-muenchen.de/lehre/vorlesungen/sose_20/tensor_networks_20/skript/15-lecture-NRG-I-WilsonChain.pdf` Tensor Networks 2020

[19] R. Bulla, T. A. Costi, and D. Vollhardt. *Finite-temperature numerical renormalization group study of the mott transition*. Phys. Rev. B, 64:045103, Jun 2001.

[20] R. Bulla, A. C. Hewson, and T. Pruschke. *Numerical renormalization group calculations for the self-energy of the impurity anderson model*. Journal of Physics: Condensed Matter, 10:8365, 1998.

[21] P. Coleman. *Introduction to Many-Body Physics*. Cambridge University Press, 2015.

[22] W. Nolting. *Grundkurs Theoretische Physik 7: Viel-Teilchen-Theorie*. Springer-Lehrbuch. Springer Berlin Heidelberg, 2014.

[23] F. Schwabl *Quantenmechanik für Fortgeschrittene (QM II)*. Springer-Lehrbuch. Springer Berlin Heidelberg, 2008.

[24] A. Altland and B. D. Simons *Condensed Matter Field Theory*. Cambridge University Press, 2010.

Erklärung

Hiermit erkläre ich, die vorliegende Arbeit selbständig verfasst zu haben und keine anderen als die in der Arbeit angegebenen Quellen und Hilfsmittel benutzt zu haben.

München, den 29. September 2020

Navid Roshani